

1 LEVERAGING MULTI-MESSENGER ASTROPHYSICS FOR DARK MATTER SEARCHES

By

Daniel Nicholas Salazar-Gallegos

A DISSERTATION

Submitted to
Michigan State University
in partial fulfillment of the requirements
for the degree of

Physics—Doctor of Philosophy
Computational Mathematics in Science and Engineering—Dual Major

Today

ABSTRACT

3 I did Dark Matter with HAWC and IceCube. I also used Graph Neural Networks

⁴ Copyright by

⁵ DANIEL NICHOLAS SALAZAR-GALLEGOS

⁶ Today

ACKNOWLEDGMENTS

8 I love my friends. Thanks to everyone that helped me figure this out. Amazing thanks to the people
9 at LANL who supported me. Eames, etc Dinner Parties Jenny and her child Kaydince Kirsten, Pat,
10 Andrea Family. You're so far but so critical to my formation. Unconditional love. Roommate

TABLE OF CONTENTS

12	LIST OF TABLES	vii
13	LIST OF FIGURES	viii
14	LIST OF ABBREVIATIONS	xii
15	CHAPTER 1 INTRODUCTION	1
16	CHAPTER 2 DARK MATTER IN THE COSMOS	2
17	2.1 Introduction	2
18	2.2 Dark Matter Basics	3
19	2.3 Evidence for Dark Matter	4
20	2.4 Searching for Dark Matter: Particle DM	11
21	2.5 Sources for Indirect Dark Matter Searches	16
22	2.6 Multi-Messenger Dark Matter	18
23	CHAPTER 3 MULTIMESSENGER ASTROPHYSICS: DETECTING HIGH EN-	
24	ERGY NEUTRAL MESSENGERS	21
25	3.1 Introduction	21
26	3.2 Charged Particles in a Medium	21
27	3.3 Photons (γ)	22
28	3.4 Neutrinos (ν)	22
29	3.5 Opportunities to Combine for Dark Matter	22
30	CHAPTER 4 HIGH ALTITUDE WATER CHERENKOV (HAWC) OBSERVATORY .	24
31	4.1 The Detector	24
32	4.2 Events Reconstruction and Data Acquisition	24
33	4.3 Remote Monitoring	24
34	CHAPTER 5 ICECUBE NEUTRINO OBSERVATORY	25
35	5.1 The Detector	25
36	5.2 Events Reconstruction and Data Acquisition	25
37	5.3 Northern Test Site	25
38	CHAPTER 6 COMPUTATIONAL TECHNIQUES IN PARTICLE ASTROPHYSICS .	26
39	6.1 Neural Networks for Gamma/Hadron Separation	26
40	6.2 Parallel Computing for Dark Matter Analyses	26
41	CHAPTER 7 GLORY DUCK: MULTI-WAVELENGTH SEARCH FOR DARK MATT-	
42	TER ANNIHILATION TOWARDS DWARF SPHEROIDAL GALAX-	
43	IES	27
44	7.1 Introduction	27
45	7.2 Dataset and Background	28
46	7.3 Analysis	30

47	7.4	HAWC Results	35
48	7.5	Glory Duck Combined Results	36
49	7.6	Appendix: HAWC Systematics	40
50	7.7	<i>J</i> -factor distributions	44
51	7.8	Discussion and Conclusions	47
52	CHAPTER 8	NU DUCK	51
53	CHAPTER 9	MULTITHREADING HAWC ANALYSES FOR DARK MATTER	
54		SEARCHES	52
55	BIBLIOGRAPHY		53

LIST OF TABLES

<p>57 Table 7.1 Summary of the relevant properties of the dSphs used in the present work. 58 Column 1 lists the dSphs. Columns 2 and 3 present their heliocentric distance 59 and galactic coordinates, respectively. Columns 4 and 5 report the J-factors of 60 each source given from the \mathcal{GS} and \mathcal{B} independent studies and their estimated 61 $\pm 1\sigma$ uncertainties. The values $\log_{10} J$ (\mathcal{GS} set) [33] correspond to the mean 62 J-factor values for a source extension truncated at the outermost observed star. 63 The values $\log_{10} J$ (\mathcal{B} set) [34] are provided for a source extension at the tidal 64 radius of each dSph. Bolded sources are within HAWC's field of view and 65 provided to the Glory Duck analysis.</p> 32
<p>66 Table 7.2 Summary of dSph observations by each experiment used in this work. A 67 ‘-’ indicates the experiment did not observe the dSph for this study. For 68 Fermi-LAT, the exposure at 1 GeV is given. For HAWC, $\Delta\theta$ is the absolute 69 difference between the source declination and HAWC latitude. HAWC is more 70 sensitive to sources with smaller $\Delta\theta$. For IACTs, we show the zenith angle 71 range, the total exposure, the energy range, the angular radius θ of the signal or 72 ON region, the ratio of exposures between the background-control (OFF) and 73 signal (ON) regions (τ), and the significance of gamma-ray excess in standard 74 deviations, σ.</p> 33
<p>75 Proof I know how to include</p>	

LIST OF FIGURES

77	Figure 2.1	Rotation curve fit to NGC 6503 from [7]. Dashed line is the contribution 78 from visible matter. Dotted curves are from gas. Dash-dot curves are from 79 dark matter (DM). Solid line is the composite contribution from all matter 80 and DM sources. Data are indicated with bold dots with error bars. Data 81 agree strongly with a matter + DM composite prediction.	5
82	Figure 2.2	Light from distant galaxy is bent in unique ways depending on the distribution 83 of mass between the galaxy and Earth. Yellow dashed lines indicate where 84 the light would have gone if the matter were not present [8].	7
85	Figure 2.3	(left) Optical image of galactic cluster 1E0657-558. (right) X-ray image of the 86 cluster with redder meaning hotter and higher baryon density. (both) Green 87 contours are reconstruction of gravity contours from weak lensing. White 88 rings are the best fit mass maxima at 68.3%, 95.5%, and 99.7% confidence. 89 The matter maxima of the clusters are clearly separated from x-ray maxima. [9]	8
90	Figure 2.4	Plank CMB sky. Sky map features small variations in temperature in primor- 91 dial light. These anisotropies are used to make inferences about the universe's 92 energy budget and developmental history. [10]	9
93	Figure 2.5	Observed Cosmic Microwave Background power spectrum as a function of 94 multipole moment from Plank [10]. Blue line is best fit model from Λ CDM. 95 Red points and lines are data and error, respectively.	10
96	Figure 2.6	Predicted power spectra of CMB for different $\Omega_m h^2$ values for fixed baryon 97 density from [11]. (left) Low $\Omega_m h^2$ increases the prominence of first and 98 second peaks. (middle) $\Omega_m h^2$ is most similar to the observed power spectrum. 99 The second and third peaks are similar in height. (right) $\Omega_m h^2$ is large which 100 suppresses the first peak and raises the prominence of the third peak.	10
101	Figure 2.7	The Standard Model (SM) of particle physics. Figure taken from http://www.quantumdiaries.org/2014/03/14/the-standard-model-a-beautiful-but-flawed-theory/	12
104	Figure 2.8	Simplified Feynman diagram demonstrating with different ways DM can 105 interact with SM particles. The 'X's refer to the DM particles whereas the 106 SM refer to fundamental particles in the SM. The large circle in the center 107 indicates the vertex of interaction and is purposely left vague. The colored 108 arrows refer to different directions of time as well as their respective labels. 109 The arrows indicate the initial and final state of the DM -SM interaction in time.	13

110	Figure 2.9 A single jet event in ATLAS detector from 2017 [16]. Jet momentum was 111 observed to be 1.9 TeV. Missing transverse momentum was observed to be 112 1.9 TeV compared to the initial transverse momentum of the event was 0. 113 Implied MET is traced by a red dashed line in event display.	14
114	Figure 2.10 More detailed pseudo-Feynman diagram of particle cascade from dark matter 115 annihilation into 2 quarks. The quarks hadronize and down to stable particles 116 like γ or the anti-proton (p^-). Diagram pulled from ICRC 2021 presentation 117 on DM annihilation search [17].	15
118	Figure 2.11 Dark Matter (DM) decay spectrum for $b\bar{b}$ initial state and γ final state. Redder 119 spectra are for larger DM masses. Bluer spectra are light DM masses. x is a 120 unitless factor defined as the ratio of the mass of DM, m_χ , and the final state 121 particle energy E_γ . Figure from [19].	17
122	Figure 2.12 Different dark matter density profiles compared. Some models produce ex- 123 ceptionally large densities at small r [20].	18
124	Figure 2.13 The Milky Way Galaxy in photons (γ) and neutrinos (ν) [22]. The Galactic 125 center is at $l=0^\circ$ and is the brightest region in all panels. (top) An Optical 126 color image of the Milky Way galaxy seen from Earth. Clouds of gas and dust 127 obscure some light from stars. (2nd down) Integrated flux of γ -rays observed 128 by the Fermi-LAT telescope [23]. (middle) Expected neutrino emission 129 that corresponds with Fermi-LAT observations. (2nd up) Expected neutrino 130 emission profile after considering detector systematics of IceCube. (bottom) 131 Observed neutrino emission from region of the galactic plane. Substantial 132 neutrino emission was detected.	19
133	Figure 2.14 Dark Matter annihilation spectra for different final state particle and standard 134 model annihilation channels [24]. Photons (red), e^\pm (green), \bar{p} (blue), ν (black).	20
135	Figure 3.1 TODO: Show a nuclear reactor with cherenkov radiation[NEEDS A SOURCE][FACT 136 CHECK THIS]	22
137	Figure 3.2 TODO: absorption spectrum of liquid and solid water[NEEDS A SOURCE][FACT 138 CHECK THIS]	23

139	Figure 7.1 [NEEDS A SOURCE] Sensitivities of five gamma-ray experiments compared 140 to percentages of the Crab nebula's emission and dark matter annihilation. 141 Solid lines present estimated sensitivities to power law spectra [FACT CHECK 142 THIS] for each experiment. Green lines are Fermi-LAT sensitivities where 143 lighter green is the sensitivity to the galactic center and light green is its sen- 144 sitivity to higher declinations. Orange, red, and purple solid lines represent 145 the MAGIC, HESS, and VERITAS 50 hour sensitivities respectively. The 146 maroon and brown lines are the HAWC 1 year and 5 year sensitivities. Across 147 four decades of gamma-ray energy, these experiments have similar sensitiv- 148 ities on the order 10^{-12} erg cm $^{-2}$ s $^{-1}$. The dotted lines are estimated dark 149 matter fluxes assuming DM annihilating to bottom quarks (red), tau leptons 150 (blue), and W bosons (green). Faded grey lines outline percentage flux of the 151 Crab nebula.	27
152	Figure 7.2 Illustration of the combination technique showing a comparison between 153 $-2 \ln \lambda$ provided by four instruments (colored lines) from the observation 154 of the same dSph without any J nuisance and their sum, <i>i.e.</i> the resulting 155 combined likelihood (thin black line). According to the test statistics of 156 Equation (7.6), the intersection of the likelihood profiles with the line $-2 \ln \lambda$ 157 = 2.71 indicates the 95% C.L. upper limit on $\langle \sigma v \rangle$. The combined likeli- 158 hood (thin black line) shows a smaller value of upper limit on $\langle \sigma v \rangle$ than 159 those derived by individual instruments. We also show the uncertainties on 160 the J -factor affects the combined likelihood and degrade the upper limit on 161 $\langle \sigma v \rangle$ (thick black line). All likelihood profiles are normalized so that the 162 global minimum $\widehat{\langle \sigma v \rangle}$ is 0. We note that each profile depends on the observa- 163 tional conditions in which a target object was observed. The sensitivity of a 164 given instrument can be degraded and the upper limits less constraining if the 165 observations are performed in non optimal conditions such as a high zenith 166 angle or a short exposure time.	36
167	Figure 7.3 HAWC upper limits at 95% confidence level on $\langle \sigma v \rangle$ versus DM mass for 168 seven annihilation channels, using the set of J -factors from Ref. [32]. The 169 solid line represents the observed combined limit. Dashed lines represent 170 limits from individual dSphs.	37
171	Figure 7.4 HAWC Brazil bands at 95% confidence level on $\langle \sigma v \rangle$ versus DM mass for 172 seven annihilation channels with J -factors from \mathcal{GS} [32]. The solid line 173 represents the combined limit from 13 dSphs. The dashed line is the expected 174 limit. The green band is the 68% containment. The yellow band is the 95% 175 containment.	38

176	Figure 7.5	Upper limits at 95% confidence level on $\langle \sigma v \rangle$ in function of the DM mass for 177 eight annihilation channels, using the set of J factors from Ref. [32] (\mathcal{GS} set 178 in Table 7.1). The black solid line represents the observed combined limit, 179 the black dashed line is the median of the null hypothesis corresponding 180 to the expected limit, while the green and yellow bands show the 68% and 181 95% containment bands. Combined upper limits for each individual detector 182 are also indicated as solid, colored lines. The value of the thermal relic 183 cross-section in function of the DM mass is given as the red dotted-dashed 184 line [39].	41
185	Figure 7.6	Same as Fig. 7.5, using the set of J factors from Ref. [34, 38] (\mathcal{B} set in Table 7.1).	42
186	Figure 7.7	Comparisons of the combined limits at 95% confidence level for each of the 187 eight annihilation channels when using the J factors from Ref. [32] (\mathcal{GS} set in 188 Table 7.1), plain lines, and the J factor from Ref. [34, 38] (\mathcal{B} set in Table 7.1), 189 dashed lines. The cross-section given by the thermal relic is also indicated [39].	43
190	Figure 7.8	Comparisons of the combined limits at 95% confidence level for a point source 191 analysis and extended source using [32] \mathcal{GS} J-factor distributions and PPPC 192 [31] annihilation spectra. Shown are the limits for Segue1 which will have 193 the most significant impact on the combined limit. 6 of the 7 DM annihilation 194 channels are shown. Solid lines are extended source studies. Dashed lines 195 are point source studies. Overall, the extended source analysis improves the 196 limit by a factor of 2.	44
197	Figure 7.9	Same as Fig. 7.8 on Coma Berenices. This dSph also contributes significantly 198 to the limit. The limits are identical in this case.	45
199	Figure 7.10	Comparison of combined limits when correcting for HAWC's pointing sys- 200 tematic. All DM annihilation channels are shown. The solid black line is the 201 ratio between published limit to the declination corrected limit. The blue solid 202 line or "Combined_og" represented the limits computed for Glory Duck. The 203 solid orange line or "Combined_ad" represented the limits computed after 204 correcting for the pointing systematic.	46
205	Figure 7.11	Comparisons between the J -factors versus the angular radius for the com- 206 putation of J factors from Ref. [32] (\mathcal{GS} set in Table 7.1) in blue and for 207 the computation from Ref. [34, 38] (\mathcal{B} set in Tab. 7.1) in orange. The solid 208 lines represent the central value of the J -factors while the shaded regions 209 correspond to the 1σ standard deviation.	48
210	Figure 7.12	Comparisons between the J -factors versus the angular radius for the com- 211 putation of J factors from Ref. [32] (\mathcal{GS} set in Tab. 7.1) in blue and for the 212 computation from Ref. [34, 38] (\mathcal{B} set in Tab. 7.1) in orange. The solid 213 lines represent the central value of the J -factors while the shaded regions 214 correspond to the 1σ standard deviation.	49

LIST OF ABBREVIATIONS

- 216 **MSU** Michigan State University
217 **LANL** Los Alamos National Laboratory
218 **DM** Dark Matter
219 **SM** Standard Model
220 **HAWC** High Altitude Water Cherenkov Observatory

221

CHAPTER 1

INTRODUCTION

222 Is the text not rendering right? Ah ok it knows im basically drafting the doc still

CHAPTER 2

223

DARK MATTER IN THE COSMOS

224 **2.1 Introduction**

225 The dark matter problem can be summarized in part by the following thought experiment.

226 Let us say you are the teacher for an elementary school classroom. You take them on a field
227 trip to your local science museum and among the exhibits is one for mass and weight. The exhibit
228 has a gigantic scale, and you come up with a fun problem for your class.

229 You ask your class, "What is the total weight of the classroom? Give your best estimation to
230 me in 30 minutes, and then we'll check your guess on the scale. If your guess is within 10% of the
231 right answer, we will stop for ice cream on the way back."

232 The students are ecstatic to hear this, and they get to work. The solution is some variation of
233 the following strategy. The students should give each other their weight or best guess if they do
234 not know. Then, all they must do is add each student's weight and get a grand total for the class.
235 The measurement on the giant scale should show the true weight of the class. When comparing
236 the measured weight to your estimation, multiply the measurement by 1.0 ± 0.1 to get the $\pm 10\%$
237 tolerances for your estimation.

238 Two of your students, Sandra and Mario, return to you with a solution.

239 They say, "We weren't sure of everyone's weight. We used 65 lbs. for the people we didn't
240 know and added everyone who does know. There are 30 of us, and we got 2,000 lbs.! That's a ton!"

241 You estimated 1,900 lbs. assuming the average weight of a student in your class was 60 lbs.
242 So, you are pleased with Sandra's and Mario's answer. You instruct your students to all gather on
243 the giant scale and read off the weight together. To all your surprise, the scale reads *10,000 lbs.*!
244 10,000 is significantly more than a 10% error from 2,000. In fact, it is approximately 5 times more
245 massive than either your or your students' estimates. You think to yourself and conclude there
246 must be something wrong with the scale. You ask an employee to check the scale and verify it is
247 well calibrated. They confirm that the scale is in working order. You weigh a couple of students
248 individually to assess that the scale is well calibrated. Sandra weighs 59 lbs., and Mario weighs

249 62 lbs., typical weights for their age. You then weigh each student individually and see that their
250 weights individually do not deviate greatly from 60 lbs. So, where does all the extra weight come
251 from?

252 This thought experiment serves as an analogy to the Dark Matter problem. The important
253 substitution to make however is to replace the students with stars and the classroom with a galaxy,
254 say the Milky Way. Individually the mass of stars is well measured and defined with the Sun as our
255 nearest test case. However, when we set out to measure the mass of a collection of stars as large as
256 galaxies, our well-motivated estimation is wildly incorrect. There simply is no way to account for
257 this discrepancy except without some unseen, or dark, contribution to mass and matter in galaxies.
258 I set out in my thesis to narrow the possibilities of what this Dark Matter could be.

259 This chapter is organized like the following... **TODO: Text should look like ... Chapter x has**
260 **blah blah blah.**

261 2.2 Dark Matter Basics

262 Presently, a more compelling theory of cosmology that includes Dark Matter (DM) in order
263 to explain a variety of observations is Λ Cold Dark Matter, or Λ CDM. I present the evidence
264 supporting Λ CDM in Section 2.3 yet discuss the conclusions of the Λ CDM model here. According
265 to Λ CDM fit to observations on the Cosmic Microwave Background (CMB), DM is 26.8% of the
266 universe's current energy budget. Baryonic matter, stuff like atoms, gas, and stars, contributes to
267 4.9% of the universe's current energy budget [1, 2, 3].

268 DM is dark; it does not interact readily with light at any wavelength. DM also does not interact
269 noticeably with the other standard model forces (Strong and Weak) at a rate that is readily observed
270 [3]. DM is cold, which is to say that the average velocity of DM is below relativistic speeds [1].
271 'Hot' DM would not likely manifest the dense structures we observe like galaxies, and instead
272 would produce much more diffuse galaxies than what is observed [3, 1]. DM is old; it played a
273 critical role in the formation of the universe and the structures within it [1, 2].

274 Observations of DM have so far been only gravitational. The parameter space available to what
275 DM could be therefore is extremely broad. The broad DM parameter space is iteratively tested in

276 DM searches by supposing a hypothesis that has not yet been ruled out and performing observations
277 to test them. When the observations yield a null result, the parameter space is constrained further.
278 I present some approaches for DM searches in Section 2.4.

279 **2.3 Evidence for Dark Matter**

280 Dark Matter (DM) has been a looming problem in physics for almost 100 years. Anomalies
281 have been observed by astrophysicists in galactic dynamics as early as 1933 when Fritz Zwicky
282 noticed unusually large velocity dispersion in the Coma cluster. Zwicky's measurement was the
283 first recorded to use the Virial theorem to measure the mass fraction of visible and invisible matter
284 in celestial bodies [4]. From Zwicky in [5], "*If this would be confirmed, we would get the surprising*
285 *result that dark matter is present in much greater amount than luminous matter.*" Zwicky's and
286 others' observation did not instigate a crisis in astrophysics because the measurements did not
287 entirely conflict with their understanding of galaxies [4]. In 1978, Rubin, Ford, and Norbert
288 measured rotation curves for ten spiral galaxies [6]. Rubin et al.'s 1978 publication presented a
289 major challenge to the conventional understanding of galaxies that could no longer be dismissed by
290 measurement uncertainties. Evidence has been mounting ever since for this exotic form of matter.
291 The following subsections provide three compelling pieces of evidence in support of the existence
292 of DM.

293 **2.3.1 First Clues: Stellar Velocities**

294 Zwicky, and later Rubin, measured the stellar velocities of various galaxies to estimate their
295 virial mass. The Virial Theorem upon which these observations are interpreted is written as

$$2T + V = 0. \quad (2.1)$$

296 Where T is the kinetic energy and V is the potential energy in a self-gravitating system. The
297 classical Newton's law of gravity from stars and gas was used for gravitational potential modeled in
298 the observed galaxies:

$$V = -\frac{1}{2} \sum_i \sum_{j \neq i} \frac{m_i m_j}{r_{ij}}. \quad (2.2)$$

299 Zwicky et al. measured just the velocities of stars apparent in optical wavelengths [5]. Rubin et al.
 300 added by measuring the velocity of the hydrogen gas via the 21 cm emission line of Hydrogen [6].
 301 The velocities of the stars and gas are used to infer the total mass of galaxies and galaxy clusters
 302 via Equation (2.1). An inferred mass is obtained from the luminosity of the selected sources. The
 303 two inferences are compared to each other as a luminosity to mass ratio which typically yielded [1]

$$\frac{M}{L} \sim 400 \frac{M_{\odot}}{L_{\odot}} \quad (2.3)$$

304 M_{\odot} and L_{\odot} referring to stellar mass and stellar luminosity, respectively. These ratios clearly indicate
 305 a discrepancy in apparent light and mass from stars and gas and their velocities.

306 Rubin et al. [6] demonstrated that the discrepancy was unlikely to be an underestimation of
 307 the mass of the stars and gas. The inferred "dark" mass was up to 5 times more than the luminous
 308 mass. This dark mass also needed to extend well beyond the extent of the luminous matter.

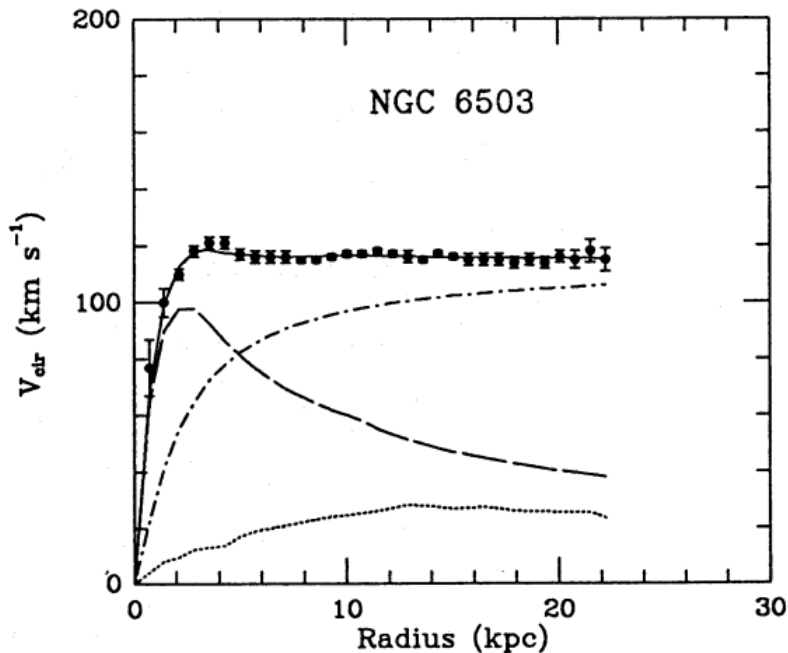


Figure 2.1 Rotation curve fit to NGC 6503 from [7]. Dashed line is the contribution from visible matter. Dotted curves are from gas. Dash-dot curves are from dark matter (DM). Solid line is the composite contribution from all matter and DM sources. Data are indicated with bold dots with error bars. Data agree strongly with a matter + DM composite prediction.

309 Figure 2.1 features one of many rotation curves plotted from the stellar velocities within galaxies.

310 The measured rotation curves mostly feature a flattening of velocities at higher radius which is not
311 expected if the gravity was only coming from gas and luminous matter. The extension of the
312 flat velocity region also indicates that the DM is distributed far from the center of the galaxy.
313 Modern velocity measurements include significantly larger objects, galactic clusters, and smaller
314 objects, dwarf galaxies. Yet, measurements along this regime are leveraging the Virial theorem
315 with Newtonian potential energies. We know Newtonian gravity is not a comprehensive description
316 of gravity. New observational techniques have been developed since 1978, and those are discussed
317 in the following sections.

318 **2.3.2 Evidence for Dark Matter: Gravitational Lensing**

319 Modern evidence for dark matter comes from new avenues beyond stellar velocities. Grav-
320 itational lensing from DM is a new channel from general relativity. General relativity predicts
321 aberrations in light caused by massive objects. In recent decades we have been able to measure the
322 lensing effects from compact objects and DM halos. Figure 2.2 shows how different massive ob-
323 jects change the final image of a faraway galaxy resulting from gravitational lensing. Gravitational
324 lensing developed our understanding of dark matter in two important ways.

325 Gravitational lensing provides additional compelling evidence for DM. The observation of two
326 merging galactic clusters in 2006, shown in Figure 2.3, provided a compelling argument for DM
327 outside the Standard Model. These clusters merged recently in astrophysical time scales. Galaxies
328 and star cluster have mostly passed by each other as the likelihood of their collision is low. Therefore,
329 these massive objects will mostly track the highest mass, dark and/or baryonic, density. Yet, the
330 intergalactic gas is responsible for the majority of the baryonic mass in the systems [4]. These gas
331 bodies will not phase through and will heat up as they collide together. The hot gas is located via
332 x-ray emission from the cluster. Two observations of the clusters were performed independently of
333 each other.

334 The first was the lensing of light around the galaxies due to their gravitational influences.
335 When celestial bodies are large enough, the gravity they exert bends space and time itself. The
336 warped space-time lenses light and will deflect in an analogous way to how glass lenses will bend

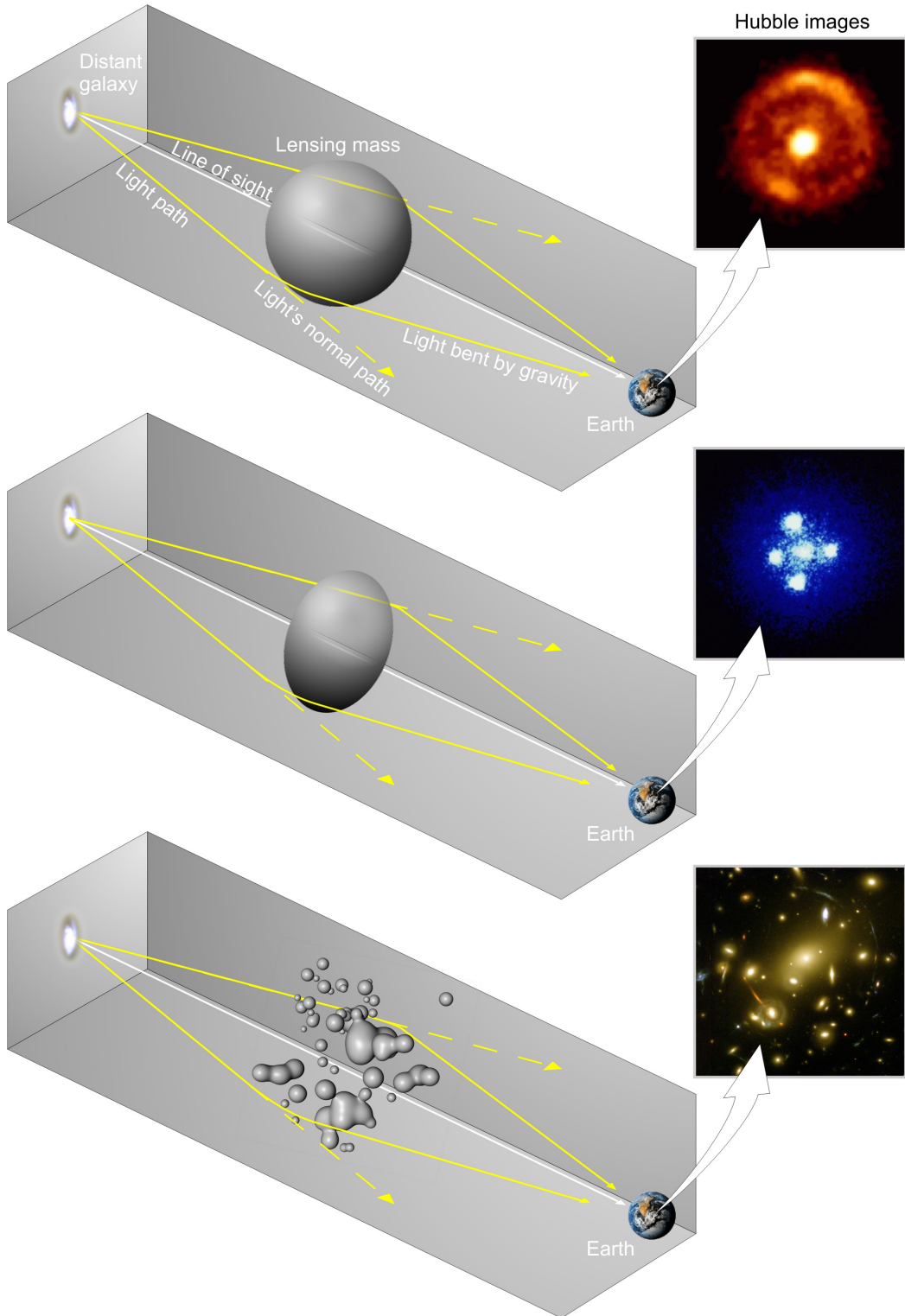


Figure 2.2 Light from distant galaxy is bent in unique ways depending on the distribution of mass between the galaxy and Earth. Yellow dashed lines indicate where the light would have gone if the matter were not present [8].

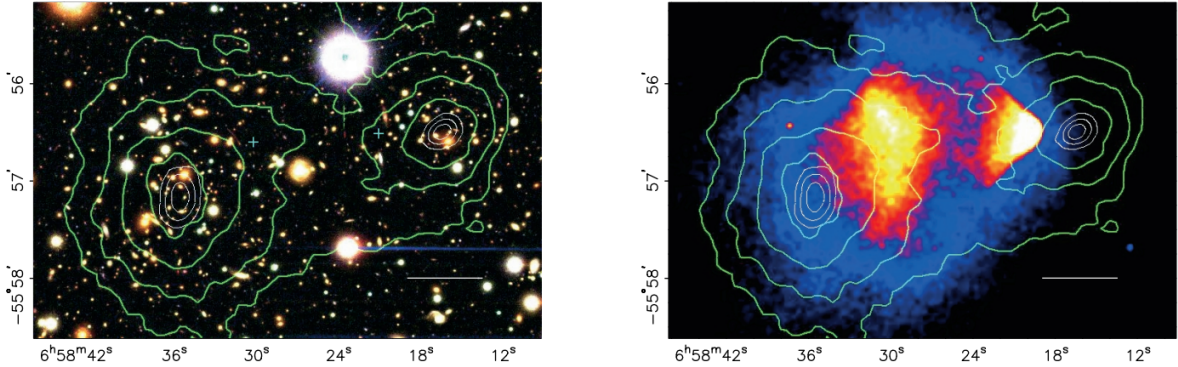


Figure 2.3 (left) Optical image of galactic cluster 1E0657-558. (right) X-ray image of the cluster with redder meaning hotter and higher baryon density. (both) Green contours are reconstruction of gravity contours from weak lensing. White rings are the best fit mass maxima at 68.3%, 95.5%, and 99.7% confidence. The matter maxima of the clusters are clearly separated from x-ray maxima. [9]

337 light, see Figure 2.2. With a sufficient understanding of light sources behind a massive object, we
 338 can reconstruct the contours of the gravitational lenses. The gradient of the contours shown in
 339 Figure 2.3 then indicates how dense the matter is and where it is.

340 The x-ray emission can then be observed from the clusters. Since these galaxies are mostly gas
 341 and are merging, then the gas should be getting hotter. If they are merging, the x-ray emissions
 342 should be the strongest where the gas is mostly moving through each other. Hence, X-ray emission
 343 maps out where the gas is in the merging galaxy cluster.

344 The lensing and x-ray observations were done on the Bullet cluster featured on Figure 2.3.
 345 The x-ray emissions do not align with the gravitational contours from lensing. The incongruence
 346 in mass density and baryon density suggests that there is a lot of matter somewhere that does
 347 not interact with light. Moreover, this dark matter cannot be baryonic [9]. The Bullet Cluster
 348 measurement did not really tell us what DM is exactly, but it did give the clue that DM also does
 349 not interact with itself very strongly. If DM did interact strongly with itself, then it would have been
 350 more aligned with the x-ray emission [9]. There have been follow-up studies of galaxy clusters with
 351 similar results. The Bullet Cluster and others like it provide a persuasive case against something
 352 possibly amiss in our gravitational theories.

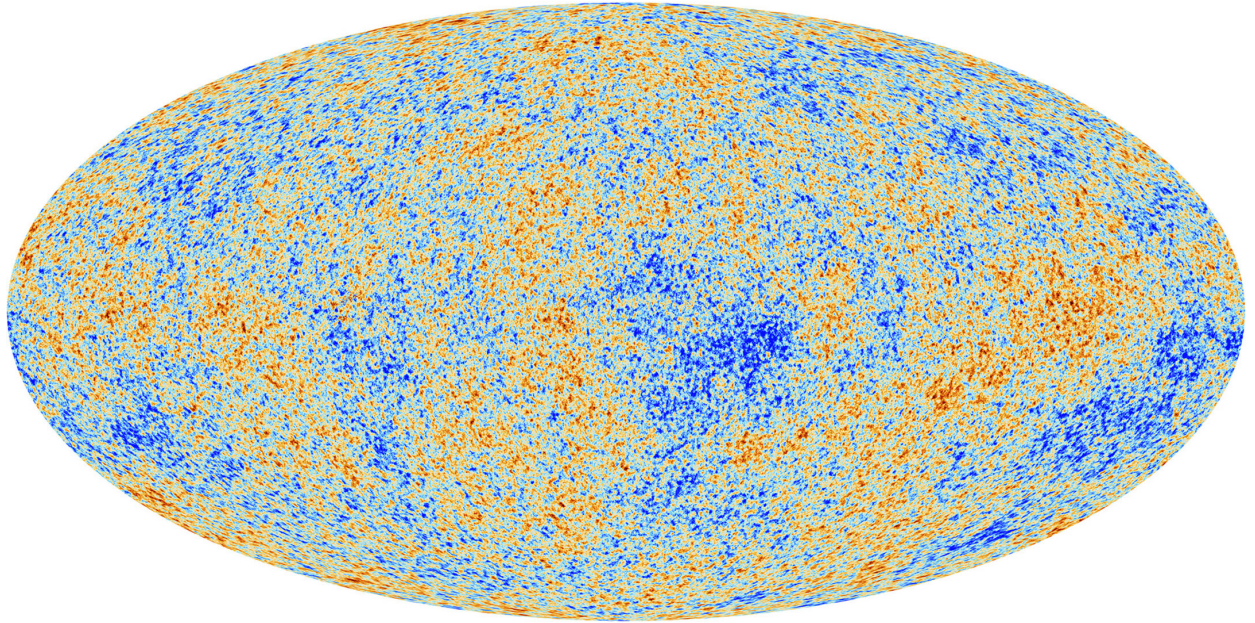


Figure 2.4 Plank CMB sky. Sky map features small variations in temperature in primordial light. These anisotropies are used to make inferences about the universe's energy budget and developmental history. [10]

353 **2.3.3 Evidence for Dark Matter: Cosmic Microwave Background**

354 The Cosmic Microwave Background (CMB) is the primordial light from the early universe
355 when Hydrogen atoms formed from the free electron and proton soup in the early universe. The
356 CMB is the earliest light we can observe; released when the universe was about 380,000 years old.
357 Then we look at how the simulated universes look like compared to what we see. Figure 2.4 is the
358 most recent CMB image from the Plank satellite after subtracting the average value and masking the
359 galactic plane [10]. Redder regions indicate a slightly hotter region in the CMB, and blue indicates
360 colder. The intensity variations are on the order of 1 in 1000 with respect to the average value.

361 The Cosmic Microwave Background shows that the universe had DM in it from an incredibly
362 early stage. To measure the DM, Dark Energy, and matter fractions of the universe from the CMB,
363 the image is analyzed into a power spectrum, which shows the amplitude of the fluctuations as
364 a function of spherical multipole moments. Λ CDM provides the best fit to the power spectra of
365 the CMB as shown in Figure 2.5. The CMB power spectrum is quite sensitive to the fraction
366 of each energy contribution in the early universe. Low l modes are dominated by variations
367 in gravitational potential. Intermediate l emerge from oscillations in photon-baryon fluid from

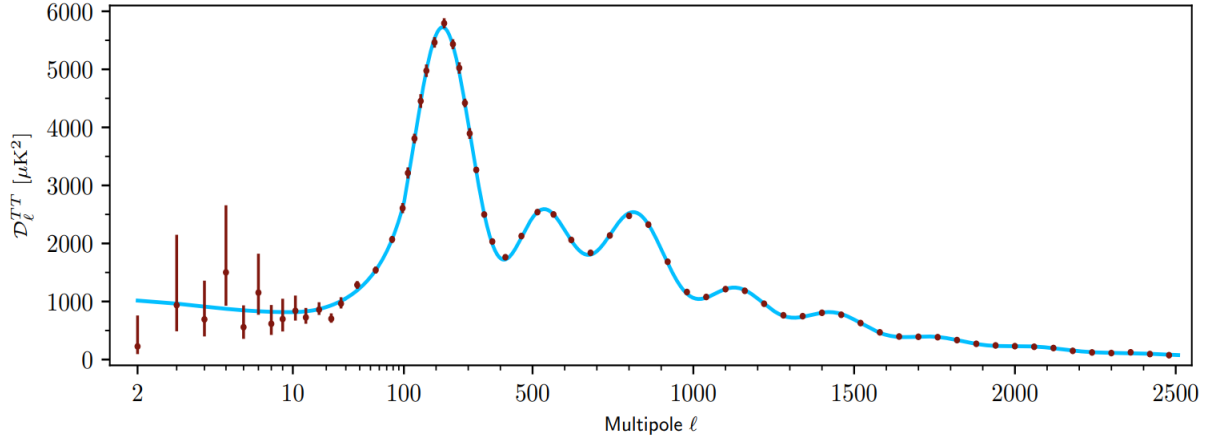


Figure 2.5 Observed Cosmic Microwave Background power spectrum as a function of multipole moment from Plank [10]. Blue line is best fit model from Λ CDM. Red points and lines are data and error, respectively.

368 competing baryon pressures and gravity. High l is a damped region from the diffusion of photons
 369 during electron-proton recombination. [1]

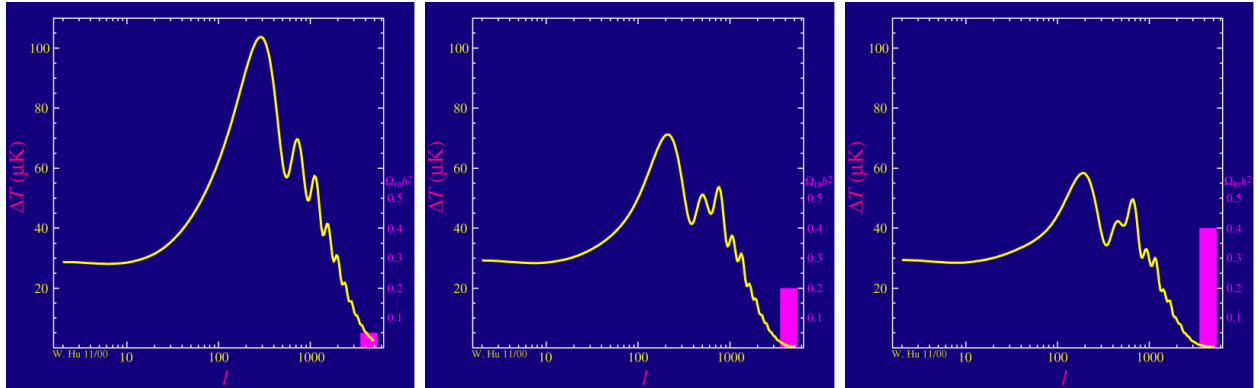


Figure 2.6 Predicted power spectra of CMB for different $\Omega_m h^2$ values for fixed baryon density from [11]. (left) Low $\Omega_m h^2$ increases the prominence of first and second peaks. (middle) $\Omega_m h^2$ is most similar to the observed power spectrum. The second and third peaks are similar in height. (right) $\Omega_m h^2$ is large which suppresses the first peak and raises the prominence of the third peak.

370 The harmonics would look quite different for a universe with less DM. Figure 2.6 demonstrates
 371 the effect $\Omega_m h^2$ has on the expected power spectrum for fixed baryon matter density. [11] Sweeping
 372 $\Omega_m h^2$ in this way clearly shows the effect dark matter has on the CMB power spectrum. The
 373 observations fit well with the Λ CDM model, and the derived fractions are as follows. The matter
 374 fraction: $\Omega_m = 0.3153$; and the baryon fraction: $\Omega_b = 0.04936$ [10]. Plank's observations also
 375 provide a measure of the Hubble constant, H_0 . H_0 especially has seen a growing tension in the

376 past decade that continues to deepened with observations from instruments like the James Webb
377 Telescope [12, 13]. As Hubble tensions deepen, we may find that perhaps Λ **CDM**, despite its
378 successes, is missing some critical physics.

379 Overall, the Newtonian motion of stars in galaxies, weak lensing from galactic clusters, and
380 power spectra from primordial light form a compelling body of research in favor of dark matter.
381 It takes another leap of theory and experimentation to make observations of DM that are non-
382 gravitational in nature. In Section 2.3, the evidence for DM implies strongly that the DM is matter
383 and not a lost parameter in the gravitational fields between massive objects. Finally, if we take one
384 axiom: that this matter has quantum behavior, such as being described by some Bohr wavelength
385 and abiding by some fermion or boson statistics; then we arrive at particle dark matter. One particle
386 DM hypothesis is the Weakly Interacting Massive Particle (WIMP). This DM candidate theory is
387 discussed further in the next section and is the focus of this thesis.

388 **2.4 Searching for Dark Matter: Particle DM**

389 Section 2.4 shows the Standard Model of particle physics and is currently the most accurate
390 model for the dynamics of fundamental particles like electrons and photons. The current status
391 of the SM does not have a viable DM candidate. When looking at the standard model, we can
392 immediately exclude any charged particle because charged particles interact strongly with light.
393 Specifically, this will rule out the following charged, fundamental particles: $e, \mu, \tau, W, u, d, s, c, t, b$
394 and their corresponding antiparticles. Recalling from Section 2.2 that DM must be long-lived and
395 stable over the age of the universe which excludes all SM particles with decay half-lives at or shorter
396 than the age of the universe. The lifetime constraint additionally eliminates the Z and H bosons.
397 Finally, the candidate DM needs to be somewhat massive. Recall from Section 2.2 that DM is cold
398 or not relativistic through the universe. This eliminates the remaining SM particles: $\nu_{e,\mu,\tau}, g, \gamma$ as
399 DM candidates. Because there are no DM candidates within the SM, the DM problem strongly
400 hints to physics beyond the SM (BSM).

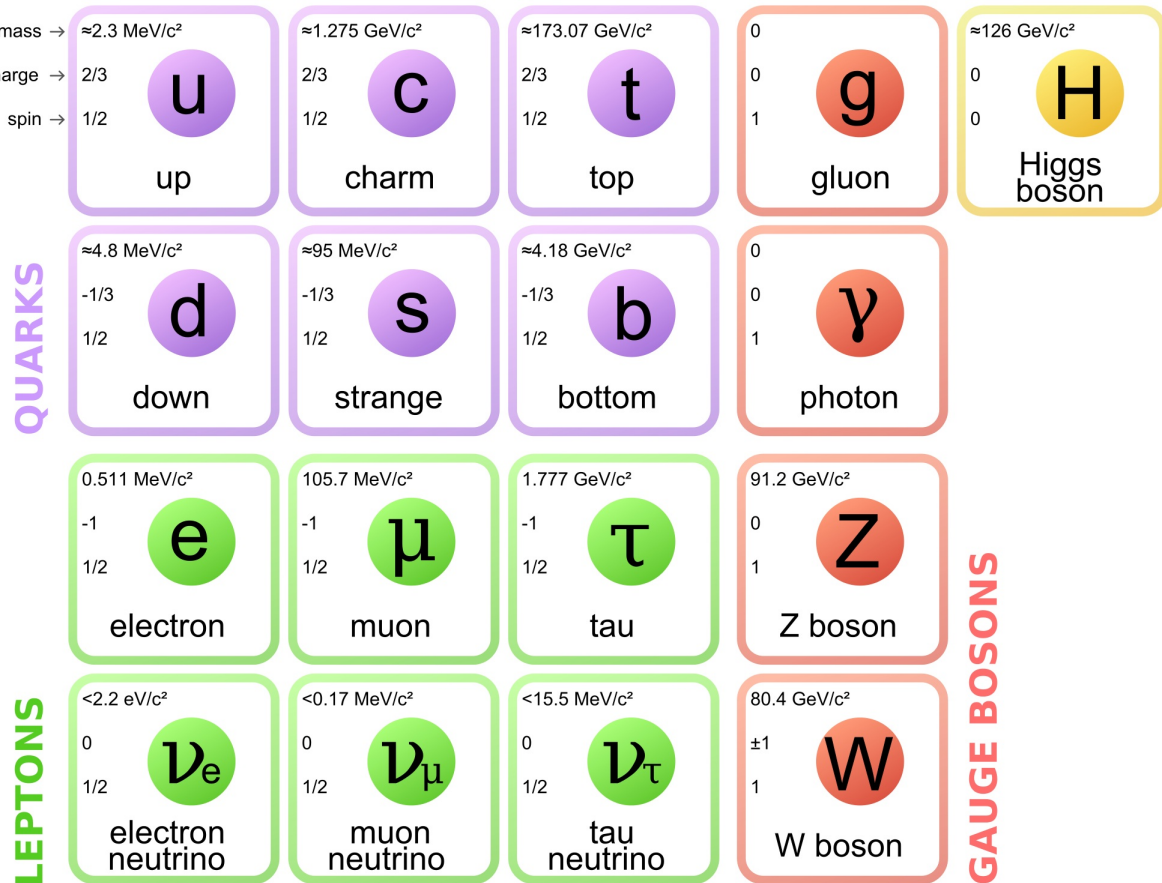


Figure 2.7 The Standard Model (SM) of particle physics. Figure taken from <http://www.quantumdiaries.org/2014/03/14/the-standard-model-a-beautiful-but-flawed-theory/>

401 2.4.1 Shake it, Break it, Make it

402 When considering DM that couples in some way with the SM, the interactions are roughly
 403 demonstrated by interaction demonstrated in Figure 2.8. The figure is a simplified Feynman
 404 diagram where the arrow of time represents the interaction modes of: **Shake it, Break it, Make it**.

405 **Shake it** refers to the direct detection of dark matter. Direct detection interactions start with
 406 a free DM particle and an SM particle. The DM and SM interact via elastic or inelastic collision
 407 and recoil away from each other. The DM remains in the dark sector and imparts some momentum
 408 onto the SM particle. The hope is that the momentum imparted onto the SM particle is sufficiently
 409 high enough to pick up with extremely sensitive instruments. Because we cannot create the DM in
 410 the lab, a direct detection experiment must wait until DM is incident on the detector. Most direct
 411 detection experiments are therefore placed in low-background environments with inert detection

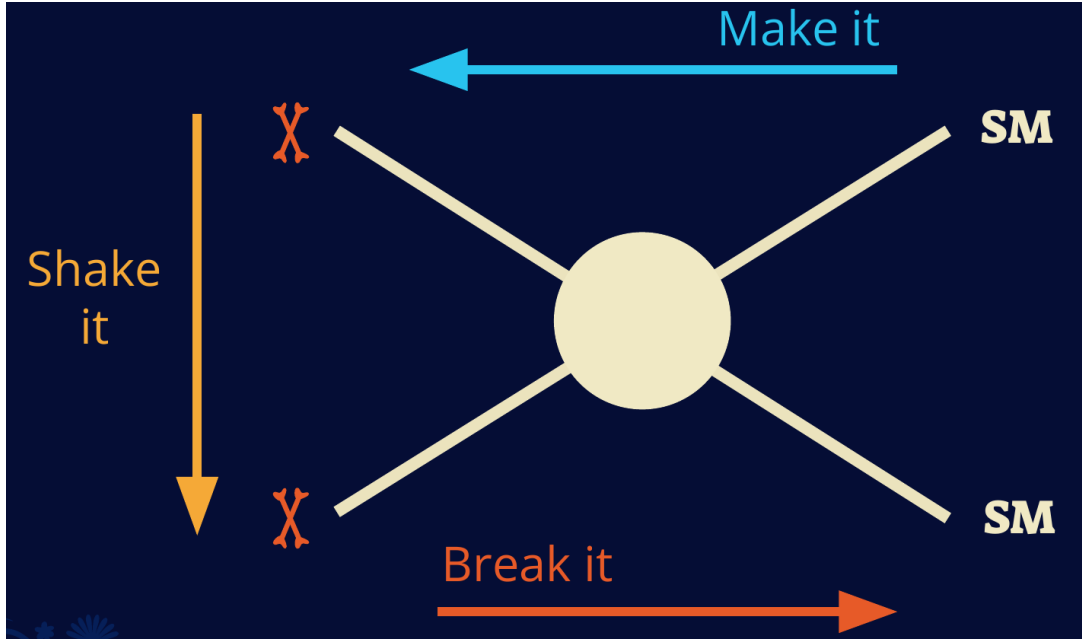


Figure 2.8 Simplified Feynman diagram demonstrating different ways DM can interact with SM particles. The 'X's refer to the DM particles whereas the SM refer to fundamental particles in the SM. The large circle in the center indicates the vertex of interaction and is purposely left vague. The colored arrows refer to different directions of time as well as their respective labels. The arrows indicate the initial and final state of the DM -SM interaction in time.

⁴¹² media like the noble gas Xenon. [14]

⁴¹³ **Make it** refers to the production of DM from SM initial states. The experiment starts with
⁴¹⁴ particles in the SM. These SM particles are accelerated to incredibly high energies and then collide
⁴¹⁵ with each other. In the confluence of energy, DM hopefully emerges as a byproduct of the SM
⁴¹⁶ annihilation. Often it is the collider experiments that are energetic enough to hypothetically produce
⁴¹⁷ DM. These experiments include the world-wide collaborations ATLAS and CMS at CERN where
⁴¹⁸ proton collide together at extreme energies. The DM searches, however, are complex. DM likely
⁴¹⁹ does not interact with the detectors and lives long enough to escape the detection apparatus of
⁴²⁰ CERN's colliders. This means any DM production experiment searches for an excess of events
⁴²¹ with missing momentum or energy in the events. An example event with missing transverse
⁴²² momentum is shown in Figure 2.9. The missing momentum with no particle tracks implies a
⁴²³ neutral particle carried the energy out of the detector. However, there are other neutral particles
⁴²⁴ in the SM, like neutrons or neutrinos, so any analysis has to account for SM signatures of missing

425 momentum. [15]

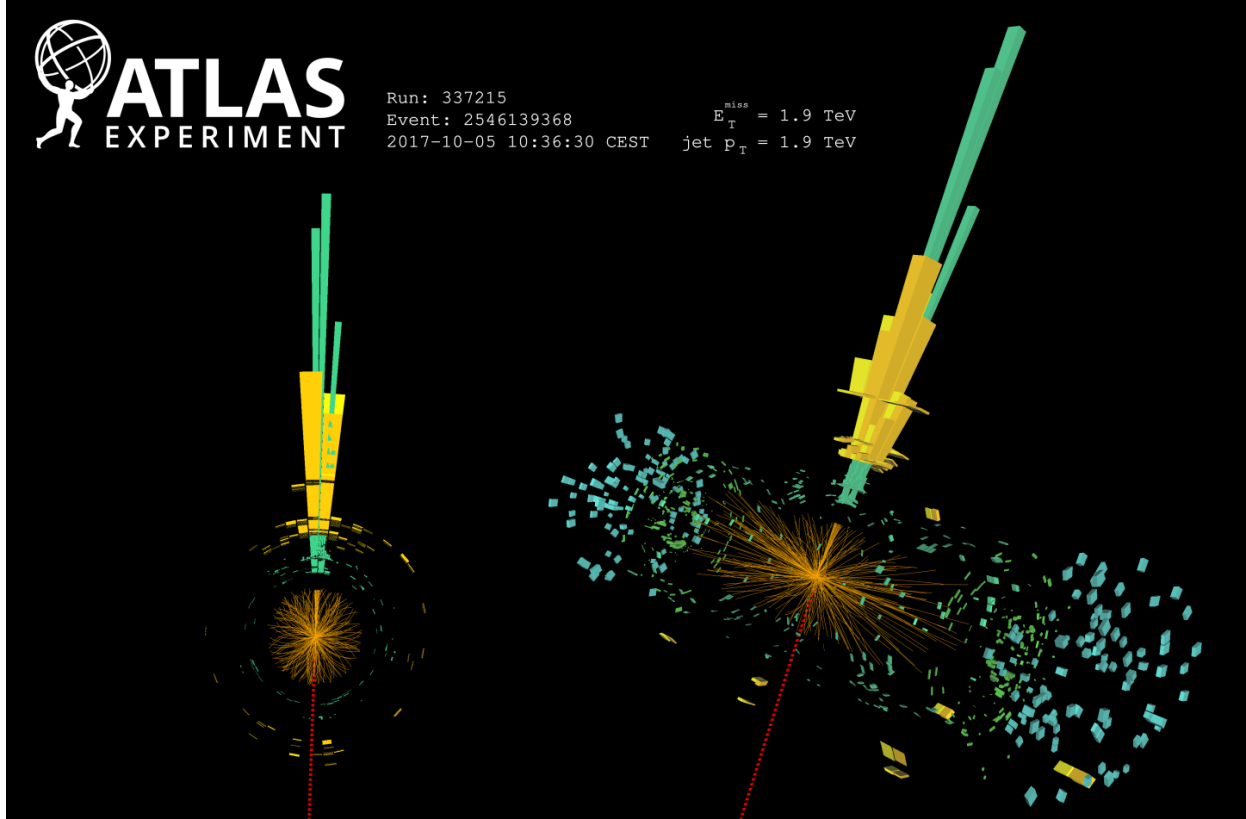


Figure 2.9 A single jet event in ATLAS detector from 2017 [16]. Jet momentum was observed to be 1.9 TeV. Missing transverse momentum was observed to be 1.9 TeV compared to the initial transverse momentum of the event was 0. Implied MET is traced by a red dashed line in event display.

426 2.4.2 Break it: Standard Model Signatures of Dark Matter through Indirect Searches

427 **Break it** refers to the creation of SM particles from the dark sector, and it is the primary focus
428 of this thesis. The interaction begins with DM or in the dark sector. The hypothesis is that this
429 DM will either annihilate with itself or decay and produce an SM byproduct. This method is
430 often referred to as the Indirect Detection of DM because we have no lab to directly control or
431 manipulate the DM. Therefore, most indirect DM searches are performed using observations of
432 known DM densities among the astrophysical sources. The strength is that we have the whole of the
433 universe and its 13.6-billion-year lifespan to use as a detector and particle accelerator. Additionally,
434 locations of dark matter are well cataloged since it was astrophysical observations that presented

435 the problem of DM in the first place.

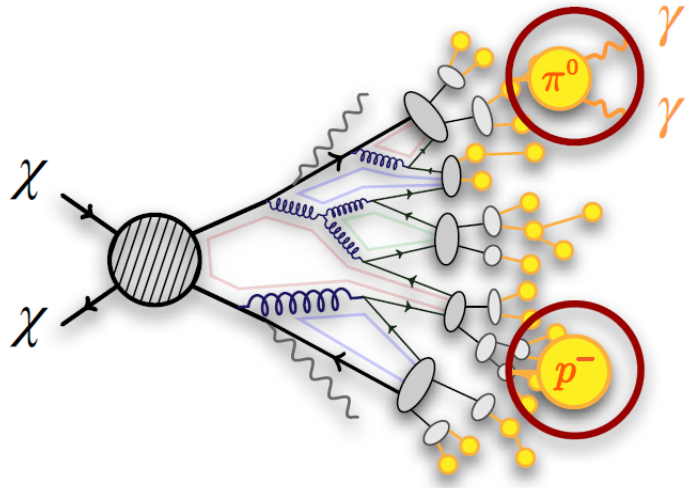


Figure 2.10 More detailed pseudo-Feynman diagram of particle cascade from dark matter annihilation into 2 quarks. The quarks hadronize and down to stable particles like γ or the anti-proton (p^-). Diagram pulled from ICRC 2021 presentation on DM annihilation search [17].

436 However, anything can happen in the universe. There are many difficult to deconvolve back-
437 grounds when searching for DM. One prominent example is the galactic center. We know the
438 galactic center has a large DM content because of stellar kinematics in our Milky Way and DM halo
439 simulations. Yet, any signal from the galactic center is challenging to parse apart from the extreme
440 environment of our supermassive black hole, unresolved sources, and diffuse emission from the
441 interstellar medium [18]. Despite the challenges, any DM model that yields evidence in the other
442 two observation methods, **Shake it or Make it** must be corroborated with indirect observations of
443 the known DM sources. Without corroborating evidence, DM observation in the lab is hard-pressed
444 to demonstrate that it is the model contributing to the DM seen at the universal scale.

445 In the case of WIMP DM, signals are described in terms of primary SM particles produced
446 from DM decay or annihilation. The SM initial state particles are then simulated down to stable
447 final states such as the γ , ν , p , or e which can traverse galactic lengths to reach Earth.

448 Figure 2.10 shows the quagmire of SM particles that emerges from SM initial states that are not
449 stable [17]. There are many SM particles with varying energies that can be produced in such an

450 interaction. For any arbitrary DM source and stable SM particle, the SM flux from DM annihilating
 451 to a neutral particle in the SM, ϕ , from a region in the sky is described by the following.

$$\frac{d\Phi_\phi}{dE_\phi} = \frac{\langle\sigma v\rangle}{8\pi m_\chi^2} \frac{dN_\phi}{dE_\phi} \times \int_{\text{source}} d\Omega \int_{l.o.s} \rho_\chi^2 dl(r, \theta') \quad (2.4)$$

452 In Equation (7.1), $\langle\sigma v\rangle$ is the velocity-weighted annihilation cross-section of DM to the SM. m_χ
 453 refers to the mass of DM, noted with Greek letter χ . $\frac{dN_\phi}{dE_\phi}$ is the N particle flux weighted by the
 454 particle energy. An example is provided in Figure 2.11 for the γ final state. The integrated terms
 455 are performed over the solid angle, $d\Omega$, and line of sight, l.o.s. ρ is the density of DM for a
 456 location (r, θ') in the sky. The terms left of the ' \times ' are often referred to as the particle physics
 457 component. The terms on the right are referred to as the astrophysical component. For decaying
 458 DM, the equation changes to...

$$\frac{d\Phi_\phi}{dE_\phi} = \frac{1}{4\pi\tau m_\chi} \frac{dN_\phi}{dE_\phi} \times \int_{\text{source}} d\Omega \int_{l.o.s} \rho_\chi dl(r, \theta') \quad (2.5)$$

459 In Equation (2.5), τ is the decay lifetime of the DM. Just as in Equation (7.1), the left and
 460 right terms are the particle physics and the astrophysical components respectively. The integrated
 461 astrophysical component of Equation (7.1) is often called the J-Factor. Whereas the integrated
 462 astrophysical component of Equation (2.5) is often called the D-Factor.

463 Exact DM $\text{DM} \rightarrow \text{SM SM}$ branching ratios are not known, so it is usually assumed to go 100%
 464 into an SM particle/anti-particle. Additionally, when a DM annihilation or decay produces one of
 465 the neutral, long-lived SM particles (ν or γ), the particle is traced back to a DM source. For DM
 466 above GeV energies, there are very few SM processes that can produce particles with such a high
 467 energy. Seeing such a signal would almost certainly be an indication of the presence of dark matter.
 468 Fortunately, the universe provides us with the largest volume and lifetime ever for a particle physics
 469 experiment.

470 2.5 Sources for Indirect Dark Matter Searches

471 The first detection of DM relied on optical observations. Since then, we have developed new
 472 techniques to find DM dense regions. As described in Section 2.3.1, many DM dense regions were
 473 through observing galactic rotation curves. Our Milky Way galaxy is among DM dense regions

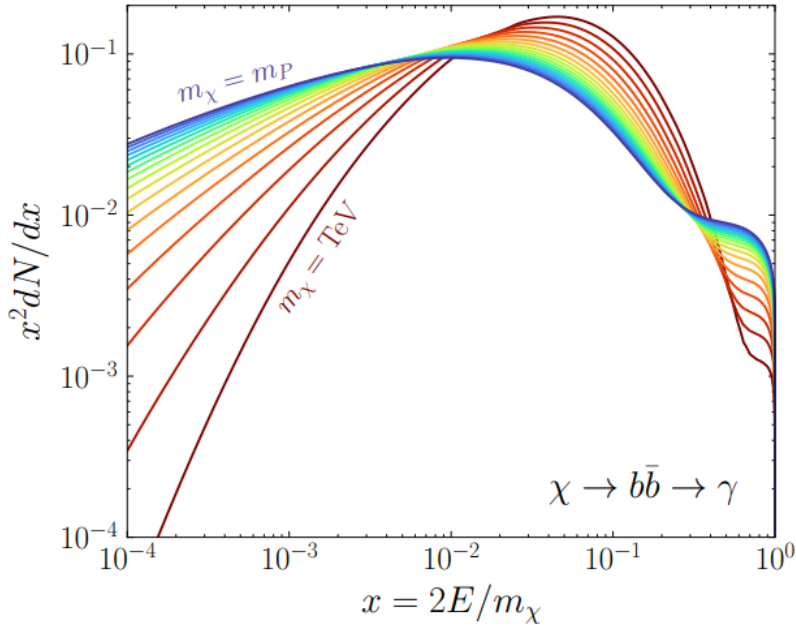


Figure 2.11 Dark Matter (DM) decay spectrum for $b\bar{b}$ initial state and γ final state. Redder spectra are for larger DM masses. Bluer spectra are light DM masses. x is a unitless factor defined as the ratio of the mass of DM, m_χ , and the final state particle energy E_γ . Figure from [19].

discovered, and it is the largest nearby DM dense region to look at. Additionally, the DM halo surrounding the Milky Way is clumpy [18]. There are regions in the DM halo of the Milky Way that have more DM than others that have captured gas over time. These sub-halos were dense enough collapse gas and form stars. These apparent sub galaxies are known as dwarf spheroidal galaxies and are the main sources studied in this thesis. Each source type comes with different trade-offs. Galactic Center studies will be very sensitive to the assumed distribution of DM. The central DM density can vary substantially as demonstrated in Figure 2.12. At distances close to the center of the galaxy, or small r , the differences in DM densities can be 3-4 orders of magnitude. Searches toward the galactic center will therefore be quite sensitive to the assumed DM distribution.

Searches toward Dwarf Spheroidal Galaxies (dSph's) suffer from uncertainties in the DM density less than the galactic center studies. This is mostly from their diminutive size being smaller than the angular resolution of most γ -ray observatories [18]. The DM content dSph's are typically determined with the Virial theorem, Equation (2.1), and are usually majority DM [18] in mass. DSph's tend to be ideal sources to look at for DM searches. Their environments are quiet with little

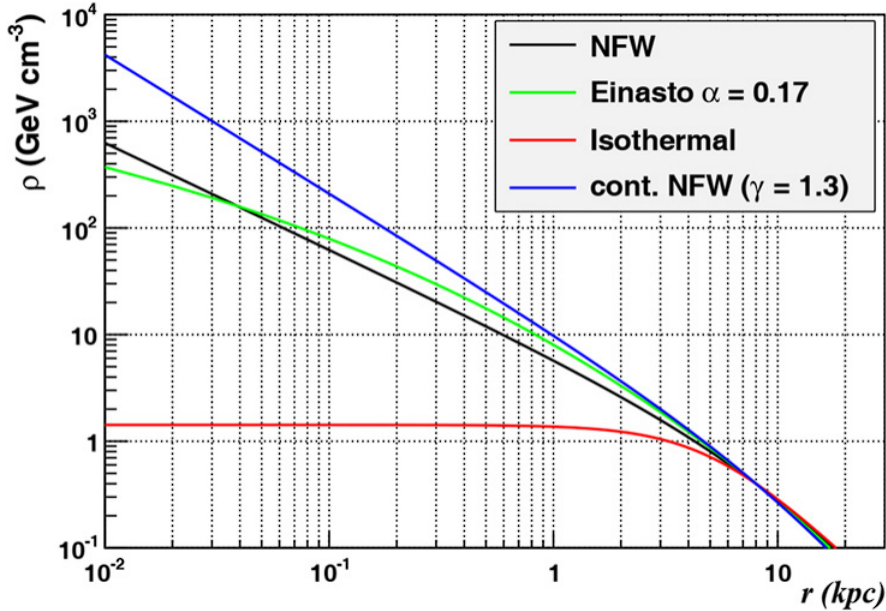


Figure 2.12 Different dark matter density profiles compared. Some models produce exceptionally large densities at small r [20].

488 astrophysical background. Unlike the galactic center, the most active components of dSph's are the
 489 stars within them versus a violent accretion disc around a black hole. All this together means that
 490 dSph's are among the best sources to look at for indirect DM searches. dSph's are the targets of
 491 focus for this thesis.

492 2.6 Multi-Messenger Dark Matter

493 Astrophysics entered a new phase in the past few decades that leverages our increasing sensitivity
 494 to SM channels and general relativity (GR). Up until the 21st century, astrophysical observations
 495 were performed with photons (γ) only. Astrophysics with this 'messenger' is fairly mature now.
 496 Novel observations of the universe have since only adjusted the sensitivity of the wavelength of
 497 light that is observed except at MeV energies. Gems like the CMB [10], and more have ultimately
 498 been observations of different wavelengths of light. Multi-messenger astrophysics proposes using
 499 other SM particles such the p^{+-} , or ν or gravitation waves predicted by general relativity.

500 The experiment LIGO had a revolutionary discovery in 2016 with the first detection of a binary
 501 black hole merger [21]. This opened the collective imagination to observing the universe through
 502 gravitational waves. There has also been a surge of interest in the neutrino (ν) sector. IceCube

503 demonstrated that we are sensitive to neutrinos in regions that correlate with significant photon
 504 emission like the galactic plane [22]. Neutrinos, like gravitational waves and light, travel mostly
 505 unimpeded from their source to our observatories. This makes pointing to the originating source
 506 of these messengers much easier than it is for cosmic rays which are deflected from their source by
 507 magnetic fields.

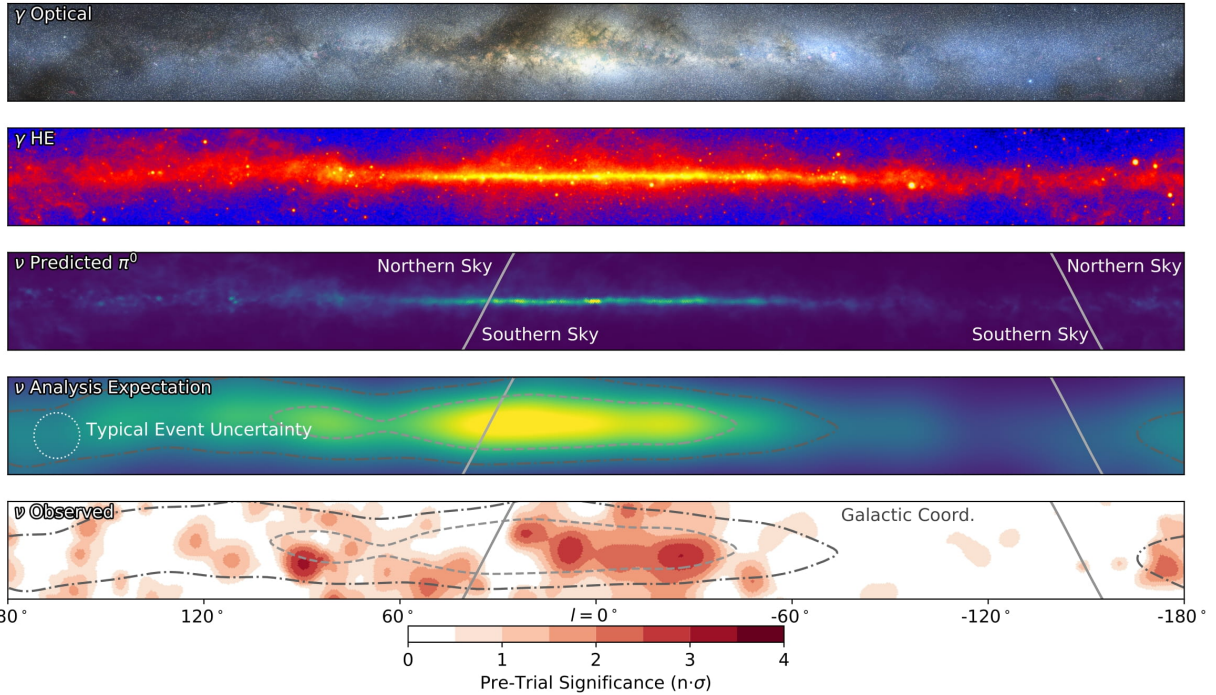


Figure 2.13 The Milky Way Galaxy in photons (γ) and neutrinos (ν) [22]. The Galactic center is at $l=0^\circ$ and is the brightest region in all panels. (top) An Optical color image of the Milky Way galaxy seen from Earth. Clouds of gas and dust obscure some light from stars. (2nd down) Integrated flux of γ -rays observed by the Fermi-LAT telescope [23]. (middle) Expected neutrino emission that corresponds with Fermi-LAT observations. (2nd up) Expected neutrino emission profile after considering detector systematics of IceCube. (bottom) Observed neutrino emission from region of the galactic plane. Substantial neutrino emission was detected.

508 The IceCube collaboration recently published a groundbreaking result of the Milky Way in
 509 neutrinos. The recent result from IceCube, shown in Figure 2.13, proves that we can make
 510 observations under different messenger regimes. The top two panels show the appearance of the
 511 galactic plane to different wavelengths of light. Some sources are more apparent in some panels,
 512 while others are not. This new channel is powerful because neutrinos are readily able to penetrate
 513 through gas and dust in the Milky Way. This new image also refines our understanding of how high

514 energy particles are produced. For example, the fit to IceCube data prefers neutrino production
 515 from the decay of π^0 [22].

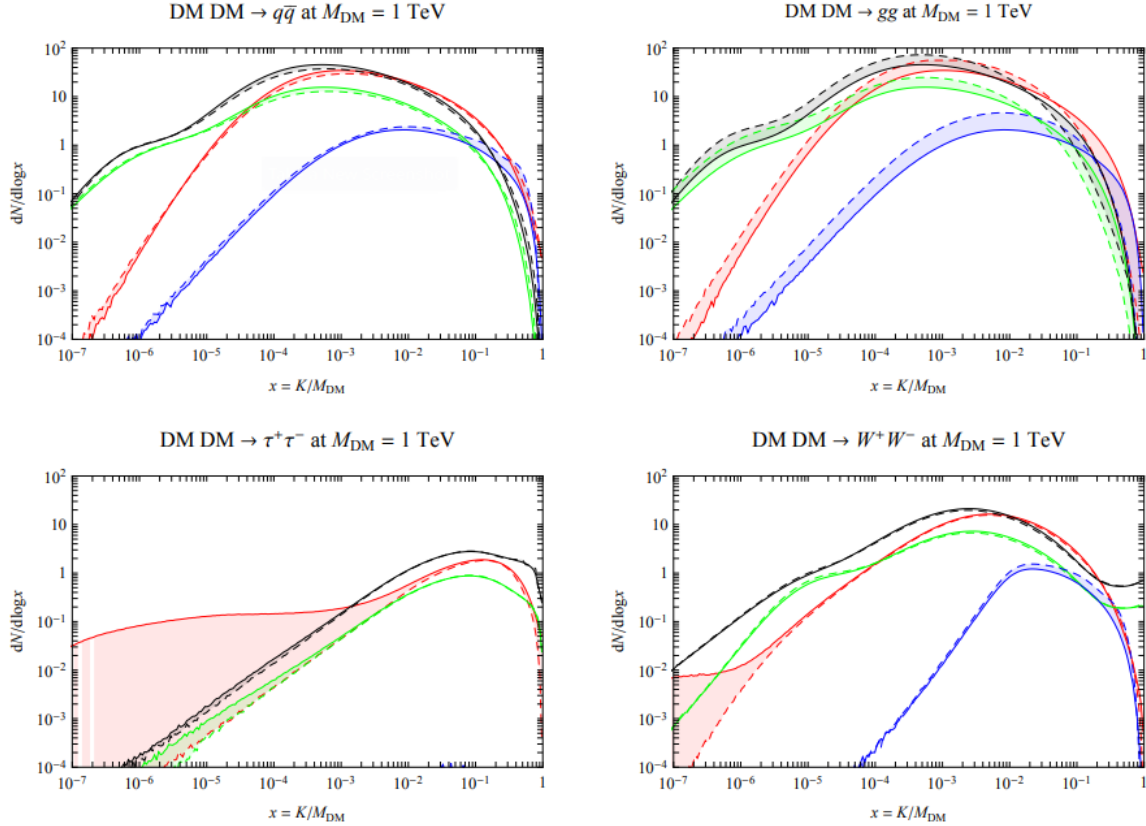


Figure 2.14 Dark Matter annihilation spectra for different final state particle and standard model annihilation channels [24]. Photons (red), e^\pm (green), \bar{p} (blue), ν (black).

516 Exposing our observations to more cosmic messengers greatly increases our sensitivity to
 517 rare processes. In the case of DM, Figure 2.14, there are many SM particles produced in DM
 518 annihilation. Among the final state fluxes are gammas and neutrinos. Charged particles are also
 519 produced however they would not likely make it to Earth since they will be deflected by magnetic
 520 fields between the source and Earth. This means observatories that can see the neutral messengers
 521 are especially good for DM searches and for combining data for a multi-messenger DM search.

CHAPTER 3

522 MULTIMESSENGER ASTROPHYSICS: DETECTING HIGH ENERGY NEUTRAL 523 MESSENGERS

524 3.1 Introduction

525 Before the 20th century, all asttrophysics observations were optical in nature. We litterly only
526 saw things with highly magnified optical observations. Then we discovered cosmic rays. cosmic
527 rays are charged particles, typically naked protons or H+. This was seen by Victor Hess in 19??.
528 Around the same time we discovered neutrinos from beta decay. Sometime around 1950 we started
529 to build neutrino detectors which were mostly sensitive to neutrinos from the sun. Finally, it was
530 theorized that compact objects like black holes and neutron stars would create waves in space-time
531 when they experience mergers or collisions.

532 In the 21st century, we have developed new observation techniques and detectors that are no only
533 sensitive to these four messengers - photons (TODO: photon), neutrinos (TODO: nu), Cosmic
534 Rays (CR), and Gravitational Wave (WV) - we're collect high energy versions of these events.
535 For the standad model particles, we're now sensitive to all messengers above the MeV eneryg
536 range. Additionally, the GW's were sensitive to are in the stellar mass black hole region and above
537 within our galactic neighborhood. This means were becoming sensitive to the fundamental physics
538 occuring within the universe and we can rely on the universe as a TeV+ particle accelerator. We
539 also have the abaility to correlate high energy events across messengers and gain new insights on
540 the processes that occur in our universe.

541 This thesis focuses on very high energy (VHE) gamma rays and neutrinos. These can both be
542 observed through the water cherenkov detection technique altho not exclusively. Methods on how
543 to detect and observe these neutral messengers are discussed Section 3.3 and Section 3.4

544 3.2 Charged Particles in a Medium

545 For high enery gamma-rays and neutrinos, we can exploit the same effect that charged particles
546 have with water. This effect is known as Cherenkov radiation. Cherenkov Radiation occurs when a
547 charged particle, usually electrons (e) or muons (μ), traverse a medium, like water, faster than the

548 speed of light in that medium. This is similar to sonic boom where an object moves through air
549 faster than the speed of sound in air. Cherenkov radiation can therefore be thought of as an 'optic
550 boom'. Many astro-particle physics experiments will use water as the medium as because water
551 has a unique set of properties ideal for charged particle tracking.



Figure 3.1 TODO: Show a nuclear reactor with cherenkov radiation[NEEDS A SOURCE][FACT CHECK THIS]

552 The frequency of light emitted due to cherenkov radiation follows the equation:

$$INSERT\ Cherenkov\ wavelength\ calc\ HERE. \quad (3.1)$$

553 The absorption spectra is shown in the following figure:

554 **3.3 Photons (γ)**

555 **3.4 Neutrinos (ν)**

556 **3.5 Opportunities to Combine for Dark Matter**



Figure 3.2 TODO: absorption spectrum of liquid and solid water[NEEDS A SOURCE][FACT CHECK THIS]

CHAPTER 4

557

HIGH ALTITUDE WATER CHERENKOV (HAWC) OBSERVATORY

558 **4.1 The Detector**

559 **4.2 Events Reconstruction and Data Acquisition**

560 **4.2.1 G/H Discrimination**

561 **4.2.2 Angle**

562 **4.2.3 Energy**

563 **4.3 Remote Monitoring**

564 **4.3.1 ATHENA Database**

565 **4.3.2 HOMER**

566

CHAPTER 5 ICECUBE NEUTRINO OBSERVATORY

567 **5.1 The Detector**

568 **5.2 Events Reconstruction and Data Acquisition**

569 **5.2.1 Angle**

570 **5.2.2 Energy**

571 **5.3 Northern Test Site**

572 **5.3.1 PIgeon remote dark rate testing**

573 **5.3.2 Bulkhead Construction**

CHAPTER 6

COMPUTATIONAL TECHNIQUES IN PARTICLE ASTROPHYSICS

575 **6.1 Neural Networks for Gamma/Hadron Separation**

576 **6.2 Parallel Computing for Dark Matter Analyses**

CHAPTER 7

GLORY DUCK: MULTI-WAVELENGTH SEARCH FOR DARK MATTER ANNIHILATION TOWARDS DWARF SPHEROIDAL GALAXIES

579 7.1 Introduction

580 The field of astrophysics now has several instruments and observatories sensitive to high
 581 energy gamma-rays. The energy sensitivity for the modern gamma-ray program spans many orders
 582 of magnitude. Figure 7.1 demonstrates these similar sensitivities across energies for the five
 583 experiments: Fermi-LAT, HAWC, HESS, MAGIC, and VERITAS.

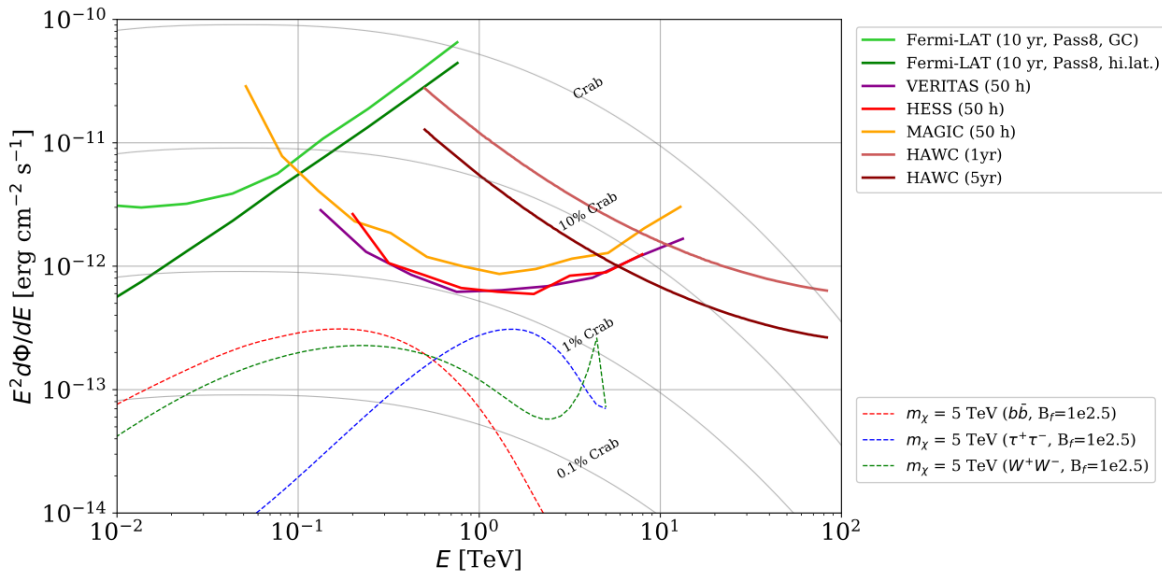


Figure 7.1 [NEEDS A SOURCE]Sensitivities of five gamma-ray experiments compared to percentages of the Crab nebula’s emission and dark matter annihilation. Solid lines present estimated sensitivities to power law spectra [FACT CHECK THIS]for each experiment. Green lines are Fermi-LAT sensitivities where lighter green is the sensitivity to the galactic center and light green is its sensitivity to higher declinations. Orange, red, and purple solid lines represent the MAGIC, HESS, and VERITAS 50 hour sensitivities respectively. The maroon and brown lines are the HAWC 1 year and 5 year sensitivities. Across four decades of gamma-ray energy, these experiments have similar sensitivities on the order 10^{-12} erg cm $^{-2}$ s $^{-1}$. The dotted lines are estimated dark matter fluxes assuming DM annihilating to bottom quarks (red), tau leptons (blue), and W bosons (green). Faded grey lines outline percentage flux of the Crab nebula.

584 Each of the five experiments featured in Figure 7.1 have independently searched for DM
 585 annihilation from dwarf galaxies and set limits. Intriguingly, their similarities overlap in regions
 586 where these observatories are less sensitive. This clearly motivates an analysis that combines data

587 from these five. Each experiment has unique gamma-ray detection methods and their weaknesses
588 and strengths can be leveraged with each other. The HAWC gamma-ray observatory is extensively
589 introduced in chapter 4, so it is not introduced here. A brief description of the remaining experiments
590 are in the following paragraphs.

591 The Large Area Telescope (LAT) is a pair conversion telescope mounted on the NASA Fermi
592 satellite in orbit 550 km above the Earth [25]. LAT's field of view covers about 20% of the
593 whole sky, and it sweeps the whole sky every 3 hours, approximately. LAT's gamma-ray energy
594 sensitivity ranges from 20 MeV up to 1 TeV. Previous DM searches towards dwarf galaxies using
595 Fermi-LAT are published in [26] and [27]

596 The High Energy Spectroscopic System (HESS), Major Atmospheric Gamma Imaging
597 Cherenkov (MAGIC), and Very Energetic Radiation Imaging Telescope Array System (VERITAS)
598 are arrays of Imaging Atmospheric Cherenkov Telescopes (IACT).

599 This chapter presents the Glory Duck analysis, the name given for the search for dark matter
600 annihilation from dwarf galaxies by combining data from the five gamma-ray observatories: Fermi-
601 LAT, HAWC, HESS, MAGIC, and VERITAS.

602 **7.2 Dataset and Background**

603 **7.2.1 Data Files**

- 604 • Detector Resolution: `response_aerie_svn_27754_systematics_best_mc_test_no`
605 `broadpulse_10pctlogchargesmearing_0.63qe_25kHzNoise_run5481_curvatu`
606 `re0_index3.root`
- 607 • Data Map: `maps-20180119/liff/maptree_1024.root`

608 **7.2.2 Data Set Chosen**

609 The maps used for this analysis contain 1017 days of data between runs 2104 (2014-11-26) and
610 7476 (2017-12-20). They were generated from pass 4.0 reconstruction. The analysis is performed
611 using the f_{hit} energy binning scheme with bins [1-9] similar to what was done for the Crab and
612 previous HAWC dSph analysis. [28, 29].

613 **7.2.3 Background Estimation**

614 This analysis was done on dwarf spheroidal (dSph) galaxies because of their large dark matter
615 (DM) content relative to baryonic. We consider the following to estimate the background to this
616 study.

617 • The dSphs are small in HAWC’s field of view, so the analysis is not sensitive to large or small
618 scale anisotropies.

619 • The dSphs used in this analysis are off the galactic plane.

620 • The dSphs are baryonically faint relative to their expected dark matter content and are not
621 expected to contain gamma-ray sources.

622 Therefor we make no additional assumptions of the background coming from our sources and
623 use HAWC’s standard direct integration method for background estimation. It is possible for gamma
624 rays from DM annihilation to scatter in transit to HAWC via Inverse Compton Scattering (ICS).
625 This was investigated and its impact on the flux is basically zero. Supporting information on this
626 is in [TODO: refer to appdx](#)

627 **7.2.4 Software Tools and Development**

628 This analysis was performed using HAL and 3ML, in Python version 2.[28, 30] Dan developed
629 a source model to implement the *Poor Particle Physicists’ Cookbook* (PPPC) [31] into HAWC
630 software. This model and corresponding Monte Carlo simulation was consolidated into a dictionary
631 for other collaborators. A NumPy version of this dictionary was made for both Py2 and Py3. The
632 code base for creating this dictionary is also in Dan’s sandbox:

- 633 • Py2: https://gitlab.com/hawc-observatory/sandboxes/salaza82/glory-duc-k-hawc/-/tree/master/GD_spectrumDictionary Generator (Deprecated)
- 635 • Py3: <https://gitlab.com/hawc-observatory/sandboxes/salaza82/pppc2dictPPPC2Dict>

637 The analysis was performed using the f_{hit} framework performed in the Crab paper[28]. The
 638 PPPC model selected for this analysis included electroweak corrections. Dictionaries for the
 639 non-electroweak model were generated but not used for this analysis. The Python2 NumPy dictio-
 640 nary file for gamma-ray final states is `dmCirSpecDict.npy`. The corresponding Python3 file is
 641 `DM_CirreelliSpectrum_dict_gammas.npy`. These files can also be used for decay channels and
 642 the PPPC describes how. [31]. Python’s pickle is not backwards compatible, so scripts run in Py3
 643 are not able to use dictionaries generated using Py2 and vice-versa.

644 All other software used for data analysis, DM profile generation, and job submission to SLURM
 645 are also kept in my sandbox for <https://gitlab.com/hawc-observatory/sandboxes/salaza82/glory-duck-hawc>the Glory Duck project. They’re broad descriptions are as follows:

- 647 • `GD_mass_profiles`: scripts that generate .fits maps for HAWC HAL according to [32].
 648 Also contains simple plots of these maps.
- 649 • `GD_spectrum`: scripts that generate NumPy dictionaries of PPPC gamma spectra [31].
- 650 • `analysis_scripts`: HAL scripts for performing likelihood computation on HAWC data or
 651 simulation with GD spectra and mass profiles.
- 652 • `pointing`: HAL scripts used to compare the impact of point systematic.
- 653 • `poisson_maps`: scripts for generating and managing poisson trials used for this study.

654 **7.3 Analysis**

655 **7.3.1 Monte Carlo Simulation**

656 The expected differential photon flux from a DM-DM annihilation to standard model particles
 657 over solid angle is described by the familiar equation.

$$\frac{d\Phi_\gamma}{dE_\gamma} = \frac{\langle\sigma v\rangle}{8\pi m_\chi^2} \frac{dN_\gamma}{dE_\gamma} \times \int_{\text{source}} d\Omega \int_{l.o.s} \rho_\chi^2 dl(r, \theta') \quad (7.1)$$

658 here $\langle \sigma v \rangle$ is the velocity weighted annihilation cross-section. $\frac{dN}{dE}$ is the expected differential number
659 of photons produced at each energy per annihilation. M_χ is the rest mass of the supposed DM
660 particle. J is the astrophysical J-factor and is defined as

661 ρ_χ is the DM density. For this value, we import the PPPC with electroweak corrections [31].
662 The spectrum is implemented as a model script in astromodels for 3ML. The J-factor profiles for
663 each source is imported from Geringer-Sameth (\mathcal{GS}) [33]. Another DM distribution model from
664 Bonnivard (\mathcal{B}) [34] was used for the complete study. However, to save computational time, limits
665 from \mathcal{GS} were scaled to \mathcal{B} instead of each experiment performing a full study a second time. We
666 create NSIDE 16384 maps of the J-factors for each dSph. These maps are integrated over every
667 spatial bin and passed to the fitting software. Plots of these maps are provided for each source in
668 the sandbox directory: `GD_mass_profiles`.

669 7.3.2 Source Selection and Annihilation Channels

670 We use many of the dSph presented in our previous dSph DM search [29]. HAWC’s sources
671 for Glory Duck include Boötes I, Coma Berenices, Canes Venatici I + II, Draco, Hercules, Leo I,
672 II, + IV, Segue 1, Sextans, and Ursa Major I + II. A full description of all sources used in Glory
673 Duck is found in Table 7.1. Triangulum II was excluded from the Glory Duck analysis because
674 of large uncertainties in its J-factor. Ursa Minor was excluded from HAWC’s contribution to the
675 combination because the source extension model extended Ursa Minor beyond HAWC’s field of
676 view. Ursa Minor was not expected to contribute significantly to the combined limit, so work was
677 not invested in a solution to include Ursa Minor.

678 The DM annihilation channels probed for the Glory Duck combination include $b\bar{b}$, $e\bar{e}$, $\mu\bar{\mu}$, $\tau\bar{\tau}$,
679 $t\bar{t}$, W^+W^- , and ZZ . A summary of all sources, with a description of each experiments’ sensitivity
680 to the source, is provided in Table 7.2.

681 7.3.3 Likelihood Methods

682 We perform a standard HAWC binned maximum likelihood analysis using f_{hit} bins 1-9. This
683 analysis was performed using HAL and 3ML, in Python2 [28, 30]. With these tools we compute
684 the max from the likelihood profiles and perform a ratio test to calculate the significance of each

Table 7.1 Summary of the relevant properties of the dSphs used in the present work. Column 1 lists the dSphs. Columns 2 and 3 present their heliocentric distance and galactic coordinates, respectively. Columns 4 and 5 report the J -factors of each source given from the \mathcal{GS} and \mathcal{B} independent studies and their estimated $\pm 1\sigma$ uncertainties. The values $\log_{10} J$ (\mathcal{GS} set) [33] correspond to the mean J -factor values for a source extension truncated at the outermost observed star. The values $\log_{10} J$ (\mathcal{B} set) [34] are provided for a source extension at the tidal radius of each dSph. **Bolded sources are within HAWC's field of view and provided to the Glory Duck analysis.**

Name	Distance (kpc)	l, b ($^{\circ}$)	$\log_{10} J$ (\mathcal{GS} set) $\log_{10}(\text{GeV}^2\text{cm}^{-5}\text{sr})$	$\log_{10} J$ (\mathcal{B} set) $\log_{10}(\text{GeV}^2\text{cm}^{-5}\text{sr})$
Boötes I	66	358.08, 69.62	$18.24^{+0.40}_{-0.37}$	$18.85^{+1.10}_{-0.61}$
Canes Venatici I	218	74.31, 79.82	$17.44^{+0.37}_{-0.28}$	$17.63^{+0.50}_{-0.20}$
Canes Venatici II	160	113.58, 82.70	$17.65^{+0.45}_{-0.43}$	$18.67^{+1.54}_{-0.97}$
Carina	105	260.11, -22.22	$17.92^{+0.19}_{-0.11}$	$18.02^{+0.36}_{-0.15}$
Coma Berenices	44	241.89, 83.61	$19.02^{+0.37}_{-0.41}$	$20.13^{+1.56}_{-1.08}$
Draco	76	86.37, 34.72	$19.05^{+0.22}_{-0.21}$	$19.42^{+0.92}_{-0.47}$
Fornax	147	237.10, -65.65	$17.84^{+0.11}_{-0.06}$	$17.85^{+0.11}_{-0.08}$
Hercules	132	28.73, 36.87	$16.86^{+0.74}_{-0.68}$	$17.70^{+1.08}_{-0.73}$
Leo I	254	225.99, 49.11	$17.84^{+0.20}_{-0.16}$	$17.93^{+0.65}_{-0.25}$
Leo II	233	220.17, 67.23	$17.97^{+0.20}_{-0.18}$	$18.11^{+0.71}_{-0.25}$
Leo IV	154	265.44, 56.51	$16.32^{+1.06}_{-1.70}$	$16.36^{+1.44}_{-1.65}$
Leo V	178	261.86, 58.54	$16.37^{+0.94}_{-0.87}$	$16.30^{+1.33}_{-1.16}$
Leo T	417	214.85, 43.66	$17.11^{+0.44}_{-0.39}$	$17.67^{+1.01}_{-0.56}$
Sculptor	86	287.53, -83.16	$18.57^{+0.07}_{-0.05}$	$18.63^{+0.14}_{-0.08}$
Segue I	23	220.48, 50.43	$19.36^{+0.32}_{-0.35}$	$17.52^{+2.54}_{-2.65}$
Segue II	35	149.43, -38.14	$16.21^{+1.06}_{-0.98}$	$19.50^{+1.82}_{-1.48}$
Sextans	86	243.50, 42.27	$17.92^{+0.35}_{-0.29}$	$18.04^{+0.50}_{-0.28}$
Ursa Major I	97	159.43, 54.41	$17.87^{+0.56}_{-0.33}$	$18.84^{+0.97}_{-0.43}$
Ursa Major II	32	152.46, 37.44	$19.42^{+0.44}_{-0.42}$	$20.60^{+1.46}_{-0.95}$
Ursa Minor	76	104.97, 44.80	$18.95^{+0.26}_{-0.18}$	$19.08^{+0.21}_{-0.13}$

Table 7.2 Summary of dSph observations by each experiment used in this work. A ‘-’ indicates the experiment did not observe the dSph for this study. For Fermi-LAT, the exposure at 1 GeV is given. For HAWC, $|\Delta\theta|$ is the absolute difference between the source declination and HAWC latitude. HAWC is more sensitive to sources with smaller $|\Delta\theta|$. For IACTs, we show the zenith angle range, the total exposure, the energy range, the angular radius θ of the signal or ON region, the ratio of exposures between the background-control (OFF) and signal (ON) regions (τ), and the significance of gamma-ray excess in standard deviations, σ .

Source name	Fermi-LAT	HAWC	H.E.S.S, MAGIC, VERITAS						
	Exposure (10^{11} s m 2)	$ \Delta\theta $ ($^\circ$)	IACT	Zenith ($^\circ$)	Exposure (h)	Energy range (GeV)	θ ($^\circ$)	τ	S (σ)
Boötes I	2.6	4.5	VERITAS	15 – 30	14.0	100–41000	0.10	8.6	-1.0
Canes Venatici I	2.9	14.6	–	–	–	–	–	–	–
Canes Venatici II	2.9	15.3	–	–	–	–	–	–	–
Carina	3.1	–	H.E.S.S.	27 – 46	23.7	310 – 70000	0.10	18.0	-0.3
Coma Berenices	2.7	4.9	H.E.S.S.	47 – 49	11.4	550 – 70000	0.10	14.4	-0.4
			MAGIC	5 – 37	49.5	60 – 10000	0.17	1.0	–
			MAGIC	29 – 45	52.1	70 – 10000	0.22	1.0	–
Draco	3.8	38.1	VERITAS	25 – 40	49.8	120 – 70000	0.10	9.0	-1.0
Fornax	2.7	–	H.E.S.S.	11 – 25	6.8	230 – 70000	0.10	45.5	-1.5
Hercules	2.8	6.3	–	–	–	–	–	–	–
Leo I	2.5	6.7	–	–	–	–	–	–	–
Leo II	2.6	3.1	–	–	–	–	–	–	–
Leo IV	2.4	19.5	–	–	–	–	–	–	–
Leo V	2.4	–	–	–	–	–	–	–	–
Leo T	2.6	–	–	–	–	–	–	–	–
Sculptor	2.7	–	H.E.S.S.	10 – 46	11.8	200 – 70000	0.10	19.8	-2.2
Segue I	2.5	2.9	MAGIC	13 – 37	158.0	60 – 10000	0.12	1.0	-0.5
			VERITAS	15 – 35	92.0	80 – 50000	0.10	7.6	0.7
Segue II	2.7	–	–	–	–	–	–	–	–
Sextans	2.4	20.6	–	–	–	–	–	–	–
Ursa Major I	3.4	32.9	–	–	–	–	–	–	–
Ursa Major II	4.0	44.1	MAGIC	35 – 45	94.8	120 – 10000	0.30	1.0	-2.1
Ursa Minor	4.1	–	VERITAS	35 – 45	60.4	160 – 93000	0.10	8.4	-0.1

685 source. This analysis is identical to the previous dSph analysis [29] except the sources are treated
 686 as extended. For the vast majority of our sources, this extension is no greater than 2 degrees. We
 687 calculate the likelihood of each source and model, assuming events are Poisson distributed, with

$$\mathcal{L} = \prod_i \frac{(B_i + S_i)^{N_i} e^{-(B_i + S_i)}}{N_i!} \quad (7.2)$$

689 S_i is the sum of expected number of signal counts. B_i is the number of background counts
 690 observed. N_i is the total number of counts. The i th bin is iterated over spatial and f_{hit} . Then we
 691 combine the profiles across all five experiments. The profile likelihood ratio λ as a function of
 692 annihilation cross-section $\langle\sigma v\rangle$ is computed by:

$$\lambda(\langle\sigma v\rangle | \mathcal{D}_{\text{dSphs}}) = \frac{\mathcal{L}(\langle\sigma v\rangle; \hat{\nu} | \mathcal{D}_{\text{dSphs}})}{\mathcal{L}(\widehat{\langle\sigma v\rangle}; \hat{\nu} | \mathcal{D}_{\text{dSphs}})} \quad (7.3)$$

693 for a considered annihilation channel and DM mass.

694 **TODO: Section pasted from paper. Rephrase cause plagiarism is a thing.** As mentioned pre-
 695 viously, each experiment computes the \mathcal{L}_{lk} from Equation (7.3) differently. The remainder of
 696 this section highlights the differences in this calculation across the experiments. Four experiments,
 697 namely *Fermi*-LAT, H.E.S.S., HAWC and MAGIC, use a binned likelihood to compute the \mathcal{L}_{lk} . For
 698 these experiments, for each observation \mathcal{D}_{lk} of a given dSph l carried out using a given gamma-ray
 699 detector k , the binned likelihood function is:

$$\mathcal{L}_{lk}(\langle\sigma v\rangle; J_l, \nu_{lk} | \mathcal{D}_{lk}) = \prod_{i=1}^{N_E} \prod_{j=1}^{N_P} \left[\mathcal{P}(s_{lk,ij}(\langle\sigma v\rangle, J_l, \nu_{lk}) + b_{lk,ij}(\nu_{lk}) | N_{lk,ij}) \right] \times \mathcal{L}_{lk,\nu}(\nu_{lk} | \mathcal{D}_{\nu_{lk}}) \quad (7.4)$$

700 where N_E and N_P are the number of considered bins in reconstructed energy and arrival
 701 direction, respectively; \mathcal{P} represents a Poisson PDF for the number of gamma-ray candidate events
 702 $N_{lk,ij}$ observed in the i -th bin in energy and j -th bin in arrival direction, when the expected number
 703 is the sum of the expected mean number of signal events s_{ij} (produced by DM annihilation) and of
 704 background events b_{ij} ; $\mathcal{L}_{lk,\nu}$ is the likelihood term for the extra ν_{lk} nuisance parameters that vary
 705 from one instrument k to another. The expected counts for signal events s_{ij} for a given dSph l and
 706 detector k is given by:

$$s_{ij}(\langle\sigma\nu\rangle, J) = \int_{E'_{\min,i}}^{E'_{\max,i}} dE' \int_{P'_{\min,j}}^{P'_{\max,j}} d\Omega' \int_0^\infty dE \int_{\Delta\Omega_{tot}} d\Omega \int_0^{T_{\text{obs}}} dt \frac{d^2\Phi(\langle\sigma\nu\rangle, J)}{dEd\Omega} \text{IRF}(E', P' | E, P, t) \quad (7.5)$$

707 where E' and E are the reconstructed and true energies, P' and P the reconstructed and true
 708 arrival directions; $E'_{\min,i}$, $P'_{\min,j}$, $E'_{\max,i}$, and $P'_{\max,j}$ are their lower and upper limits of the i -th
 709 energy bin and the j -th arrival direction bin; T_{obs} is the (dead-time corrected) total observation
 710 time; t is the time along the observations; $d^2\Phi/dEd\Omega$ is the DM flux in the source region (see
 711 Equation (7.1)); and $\text{IRF}(E', P' | E, P, t)$ is the IRF, which can be factorized as the product of the
 712 effective collection area of the detector $A_{\text{eff}}(E, P, t)$, the PDFs for the energy estimator $f_E(E' | E, t)$,
 713 and arrival direction $f_P(P' | E, P, t)$ estimators. Note that for Fermi-LAT, HAWC, MAGIC, and
 714 VERITAS the effect of the finite angular resolution is taken into account through the convolution
 715 of $d\Phi/dEd\Omega$ with f_P in Equation (7.5), whereas in the cases of H.E.S.S. f_P is approximated by a
 716 delta function. This approximation has been made in order to maintain compatibility of the result
 717 with what has been previously published. The difference introduced by this approximation is $< 5\%$
 718 for all considered dSphs. **TODO: End of paper section**

719 From Equation (7.3), we can compute the test statistic (TS) with the ratio test:

$$\text{TS} = -2 \ln \left(\frac{\mathcal{L}}{\mathcal{L}^{\max}} \right). \quad (7.6)$$

720 \mathcal{L}^{\max} here is equivalent to $\mathcal{L}(N_i, B_i, S_i = 0)$ or no signal counts.

721 7.4 HAWC Results

722 13 of the 20 dSphs considered for the Glory Duck analysis are within HAWC's field of view.
 723 These dSph are analyzed for DM content according to the likelihood method described in Sec-
 724 tion 7.3.3. The 13 likelihood profiles are then combined to create a combined limit on the dark
 725 matter cross-section. This combination is done for 7 of the 8 annihilation channels used in the Glory
 726 Duck analysis. Figure 7.3 shows the combined limit for all annihilation channels with HAWC only
 727 observations. We also perform 300 studies of Poisson trials on the background. These trials are
 728 used to produce HAWC Brazil bands are shared with the other collaborators for combined Brazil

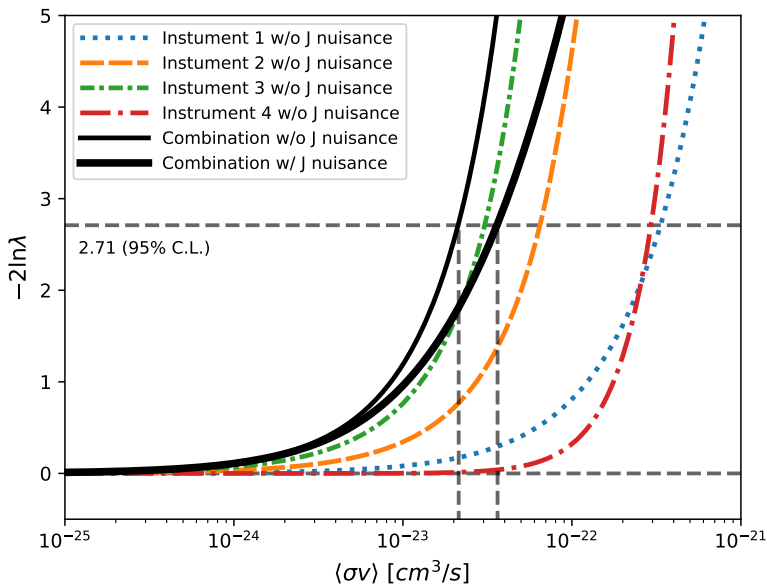


Figure 7.2 Illustration of the combination technique showing a comparison between $-2 \ln \lambda$ provided by four instruments (colored lines) from the observation of the same dSph without any J nuisance and their sum, *i.e.* the resulting combined likelihood (thin black line). According to the test statistics of Equation (7.6), the intersection of the likelihood profiles with the line $-2 \ln \lambda = 2.71$ indicates the 95% C.L. upper limit on $\langle \sigma v \rangle$. The combined likelihood (thin black line) shows a smaller value of upper limit on $\langle \sigma v \rangle$ than those derived by individual instruments. We also show the uncertainties on the J -factor affects the combined likelihood and degrade the upper limit on $\langle \sigma v \rangle$ (thick black line). All likelihood profiles are normalized so that the global minimum $\widehat{\langle \sigma v \rangle}$ is 0. We note that each profile depends on the observational conditions in which a target object was observed. The sensitivity of a given instrument can be degraded and the upper limits less constraining if the observations are performed in non optimal conditions such as a high zenith angle or a short exposure time.

729 Bands. The results on fitting to HAWC's poisson trials of the DM hypothesis is shown in Figure 7.4
 730 for seven of the DM annihilation channels.

731 No DM was found in HAWC observations. The limits are dominated by the dSph Segue1 and
 732 Coma Berenices. The remaining 11 dSphs do no contribute significantly to the limit. Even though
 733 the remaining dSphs have large J -factors, they are towards the edge of HAWC's field of view where
 734 this analysis is less sensitive.

735 7.5 Glory Duck Combined Results

736 The crux of this analysis is that HAWC's results are combined with 4 other gamma-ray obser-
 737 vatories: Fermi-LAT, H.E.S.S., MAGIC, and VERITAS. The complete joint likelihood for the l -th

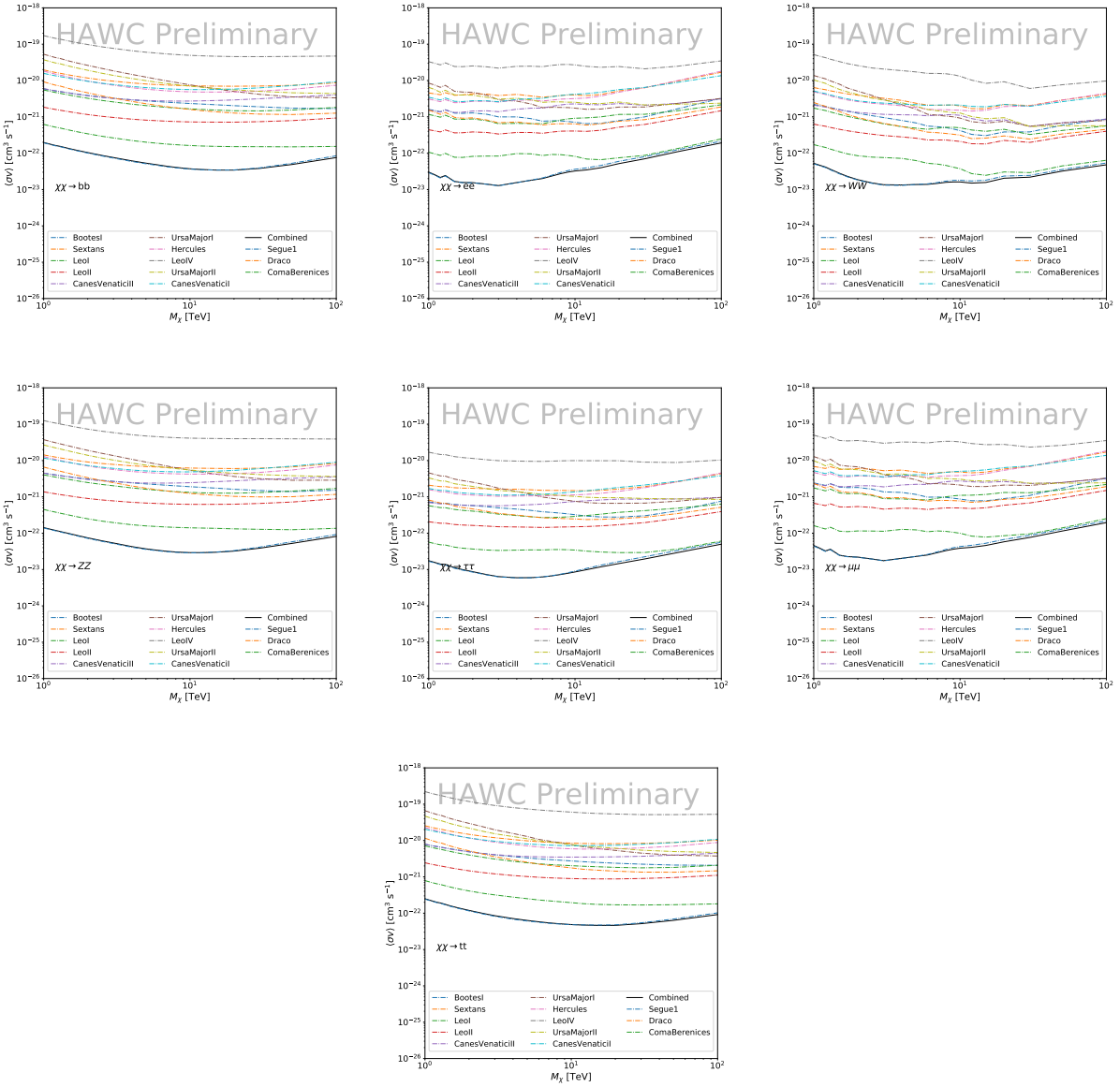


Figure 7.3 HAWC upper limits at 95% confidence level on $\langle\sigma v\rangle$ versus DM mass for seven annihilation channels, using the set of J -factors from Ref. [32]. The solid line represents the observed combined limit. Dashed lines represent limits from individual dSphs.

738 dSph is the product of likelihood functions of the 5 experiments.

739 **TODO:** place holder for results

740 No significant DM emission was observed by any of the five telescopes. We present upper

741 limits on $\langle\sigma v\rangle$ using the test statistics, Eq. (7.6).

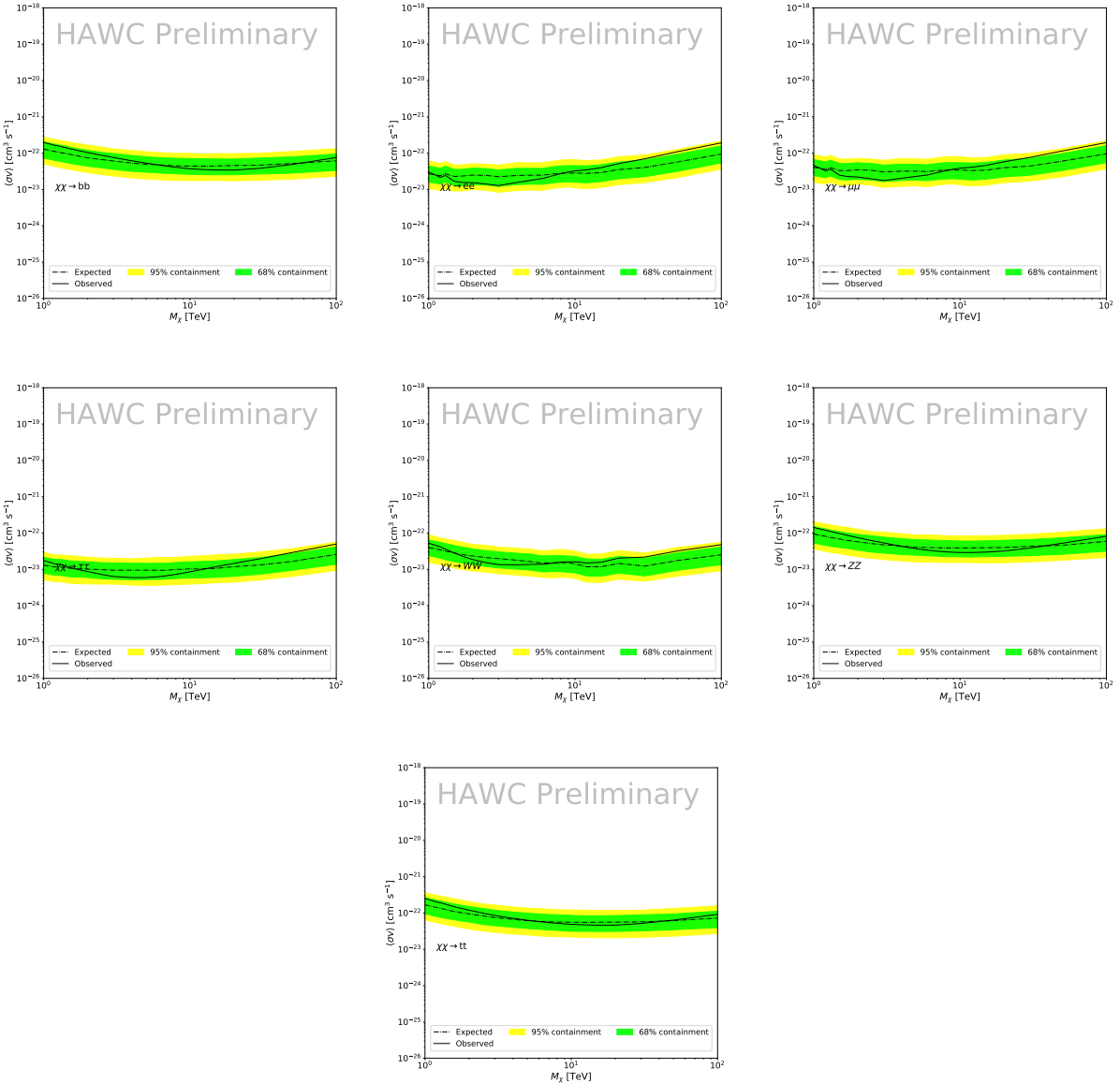


Figure 7.4 HAWC Brazil bands at 95% confidence level on $\langle\sigma v\rangle$ versus DM mass for seven annihilation channels with J -factors from \mathcal{GS} [32]. The solid line represents the combined limit from 13 dSphs. The dashed line is the expected limit. The green band is the 68% containment. The yellow band is the 95% containment.

$$TS = -2 \ln \lambda(\langle\sigma v\rangle), \quad (7.7)$$

No significant DM emission was observed by any of the five instruments. We present the upper limits on $\langle\sigma v\rangle$ assuming seven independent DM self annihilation channels, namely W^+W^- , Z^+Z^- , $b\bar{b}$, $t\bar{t}$, e^+e^- , $\mu^+\mu^-$, and $\tau^+\tau^-$. The 68% and 95% containment bands are produced from 300

745 Poisson realizations of the null hypothesis corresponding to each of the combined datasets. These
746 300 realizations are combined identically to dSph observations. The containment bands and the
747 median are extracted from the distribution of resulting limits on the null hypothesis. These 300
748 realizations are obtained either by fast simulations of the OFF observations, for H.E.S.S., MAGIC,
749 VERITAS, and HAWC, or taken from real observations of empty fields of view in the case of
750 Fermi-LAT [35, 36, 37].

751 The obtained limits are shown in Figure 7.5 for the \mathcal{GS} set of J -factors [32] and in Figure 7.6
752 for the \mathcal{B} set of J -factors [34, 38]. The combined limits are presented with their 68% and 95%
753 containment bands, and are expected to be close to the median limit when no signal is present.
754 We observe agreement with the null hypothesis for all channels, within 2σ standard deviations,
755 between the observed limits and the expectations given by the median limits. Limits obtained from
756 each detector are also indicated in the figures, where limits for all dSphs observed by the specific
757 instrument have been combined.

758 Below ~ 300 GeV, the *Fermi*-LAT dominates the DM limits for all annihilation channels. From
759 ~ 300 GeV to ~ 2 TeV, *Fermi*-LAT continues to dominate for the hadronic and bosonic DM channels,
760 yet the IACTs (H.E.S.S., MAGIC, and VERITAS) and *Fermi*-LAT all contribute to the limit for
761 leptonic DM channels. For DM masses between ~ 2 TeV to ~ 10 TeV, the IACTs dominate leptonic
762 DM annihilation channels, whereas both the *Fermi*-LAT and the IACTs dominate bosonic and
763 hadronic DM annihilation channels. From ~ 10 TeV to ~ 100 TeV, both the IACTs and HAWC
764 contribute significantly to the leptonic DM limit. For hadronic and bosonic DM, the IACTs and
765 *Fermi*-LAT both contribute strongly.

766 We notice that the limits computed using the \mathcal{B} set of J -factor are always better compared to the
767 ones calculated with the \mathcal{GS} set. For the W^+W^- , Z^+Z^- , $b\bar{b}$, and $t\bar{t}$ channels, the ratio between the
768 limits computed with the two sets of J -factor is varying between a factor of ~ 3 and ~ 5 depending
769 on the energy, with the largest ratio around 10 TeV. For the channels e^+e^- , $\mu^+\mu^-$, and $\tau^+\tau^-$, the
770 ratio lies between ~ 2 to ~ 6 , being maximum around 1 TeV. Examining Figure 7.11 and Figure 7.12
771 in Section 7.7, these differences are explained by the fact that the \mathcal{B} set provides higher J -factors

772 for the majority of the studied dSphs, with the notable exception of Segue I. The variation on the
773 ratio of the limits for the two sets is due to different dSph dominating the limits depending on the
774 energy. This pushes the range of thermal cross-section which can be excluded to higher mass. This
775 comparison demonstrates the magnitude of systematic uncertainties associated with the choice of
776 the J -factor

777 This comparison demonstrates the magnitude of systematic uncertainties associated with the
778 choice of the J -factor calculation. The \mathcal{GS} and \mathcal{B} sets present a difference in the limits for all
779 channels of about This difference is explained, see Figure 7.11 and Figure 7.12 in Appendix, by the
780 fact that the \mathcal{B} set provides higher J factors for all dSph except for Segue I. This pushes the range
781 of thermal cross-section which can be excluded to higher mass.

782 7.6 Appendix: HAWC Systematics

783 7.6.1 Inverse Compton Scattering

784 The DM-DM annihilation channels produce many high energy electrons regardless of the
785 primary annihilation channel. These high energy electrons can produce high energy gamma-rays
786 through Inverse Compton Scattering (ICS). If this effect is strong, it would change the morphology
787 of the source and increase the total expected gamma-ray counts from any source. The PPPC [31]
788 provides tools in Mathematica for calculating the impact of ICS for an arbitrary location in the
789 sky for a specified annihilation channel. We calculated the change in gamma-ray counts for DM
790 annihilation to primary $e\bar{e}$ for RA and Dec corresponding to Segue1 and Coma Berenices. These
791 dSphs were chosen because they are the strongest contributors to the limit. $e\bar{e}$ was selected because
792 it would have the largest number of high energy electrons. The effect was found to be on the order
793 of 10^{-7} on the gamma-ray spectrum. As a result, this systematic is not considered in our analysis.

794 7.6.2 Point Source Versus Extended Source Limits

795 The previous DM search toward dSph approximated the dSphs as point sources [29]. In
796 this analysis, the dSphs are implemented as extended with J-factor distributions following those
797 produced by [32]. The resolution of the cited map is much finer than HAWC's angular resolution.

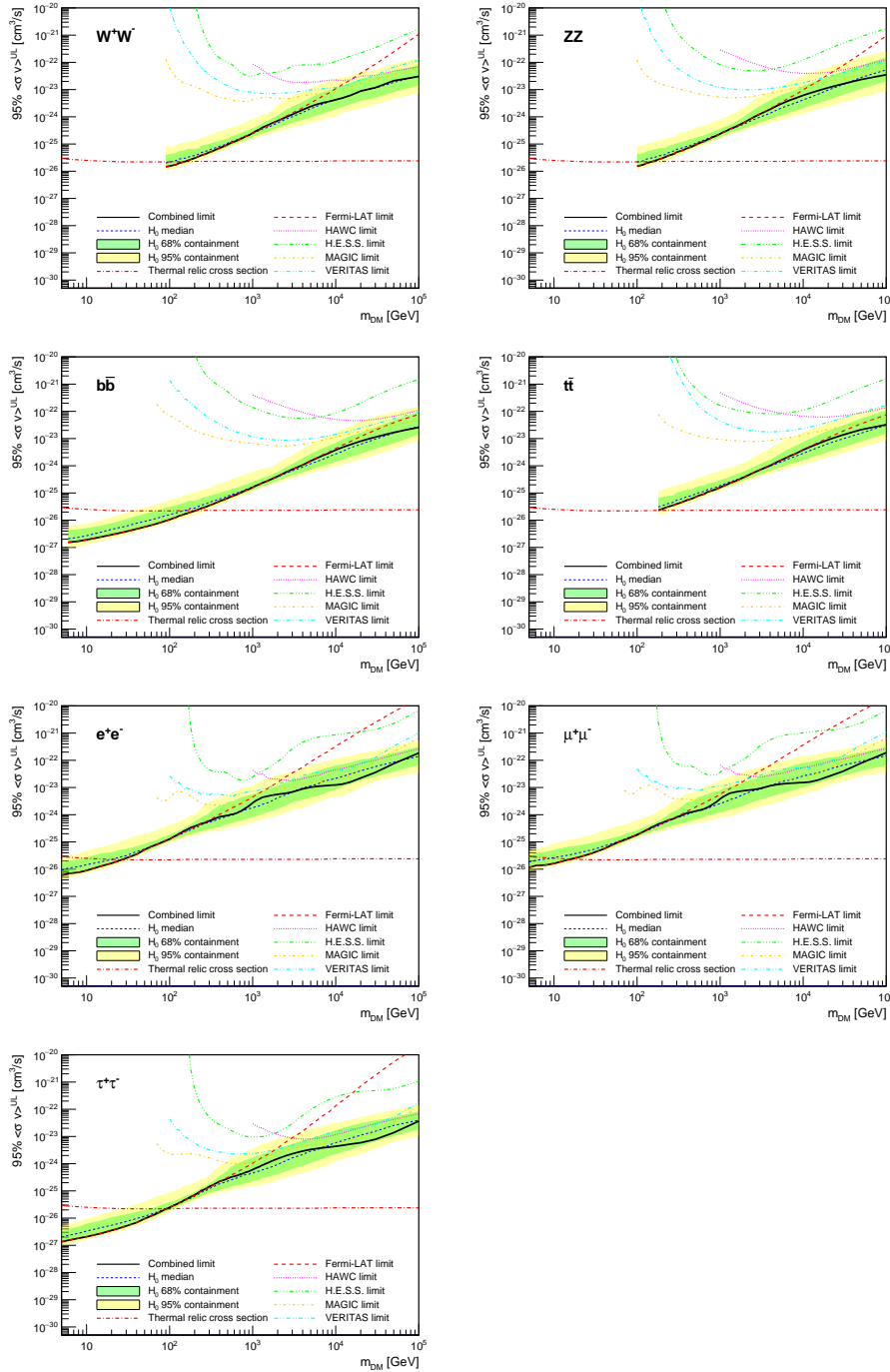


Figure 7.5 Upper limits at 95% confidence level on $\langle\sigma v\rangle$ in function of the DM mass for eight annihilation channels, using the set of J factors from Ref. [32] (\mathcal{GS} set in Table 7.1). The black solid line represents the observed combined limit, the black dashed line is the median of the null hypothesis corresponding to the expected limit, while the green and yellow bands show the 68% and 95% containment bands. Combined upper limits for each individual detector are also indicated as solid, colored lines. The value of the thermal relic cross-section in function of the DM mass is given as the red dotted-dashed line [39].

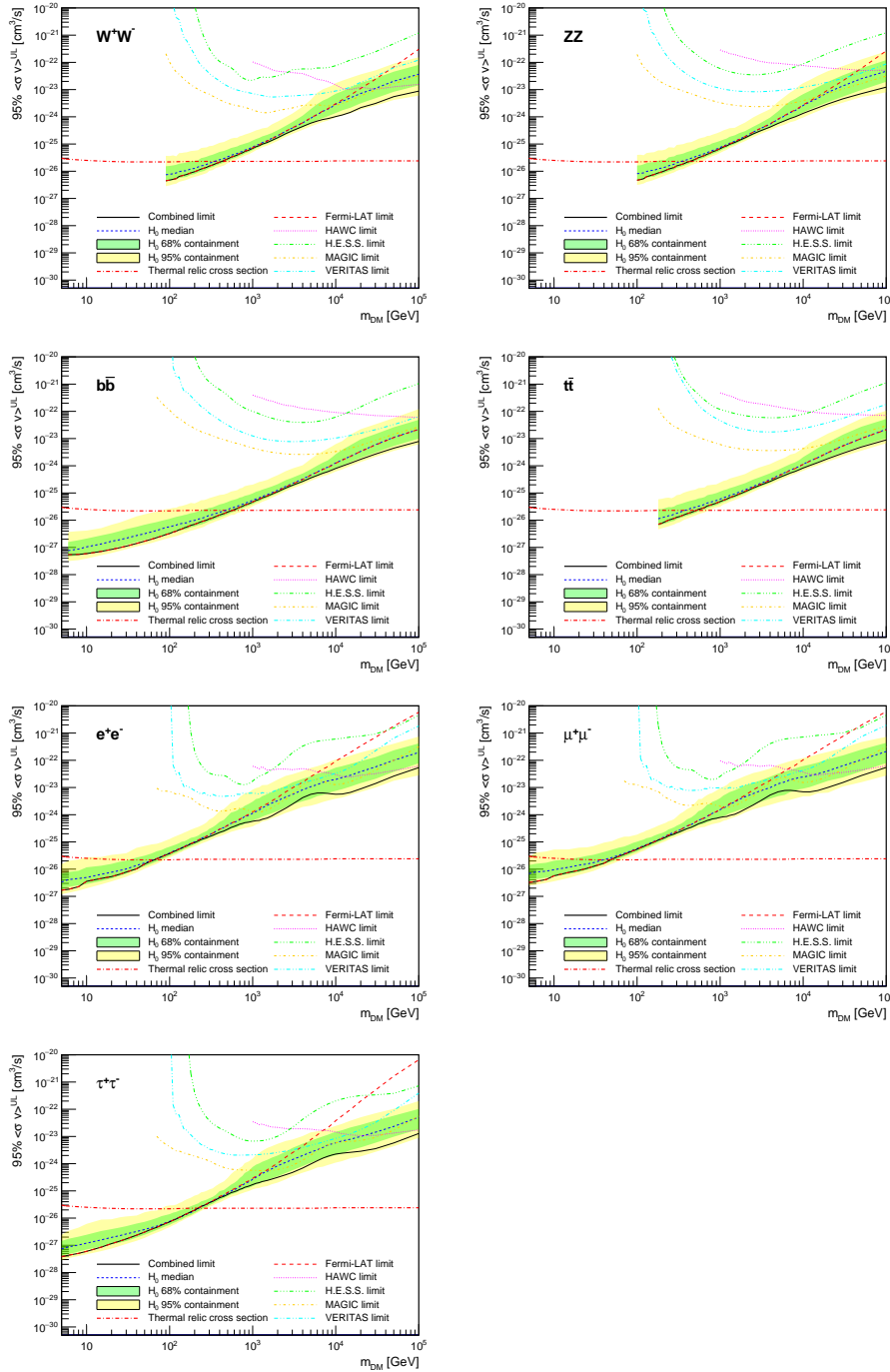


Figure 7.6 Same as Fig. 7.5, using the set of J factors from Ref. [34, 38] (\mathcal{B} set in Table 7.1).

798 The vast majority of the J-factor distribution is represented on the central HAWC pixel of the dSph
 799 spatial map. However, the neighboring 8 pixels are not negligible and contribute to our limit.

800 Figure 7.8 shows a substantial improvement to the limit for Segue1. Fig. 7.9 however showed
 801 identical limits. These disparities are best explained by the relative difference in their J-Factors.

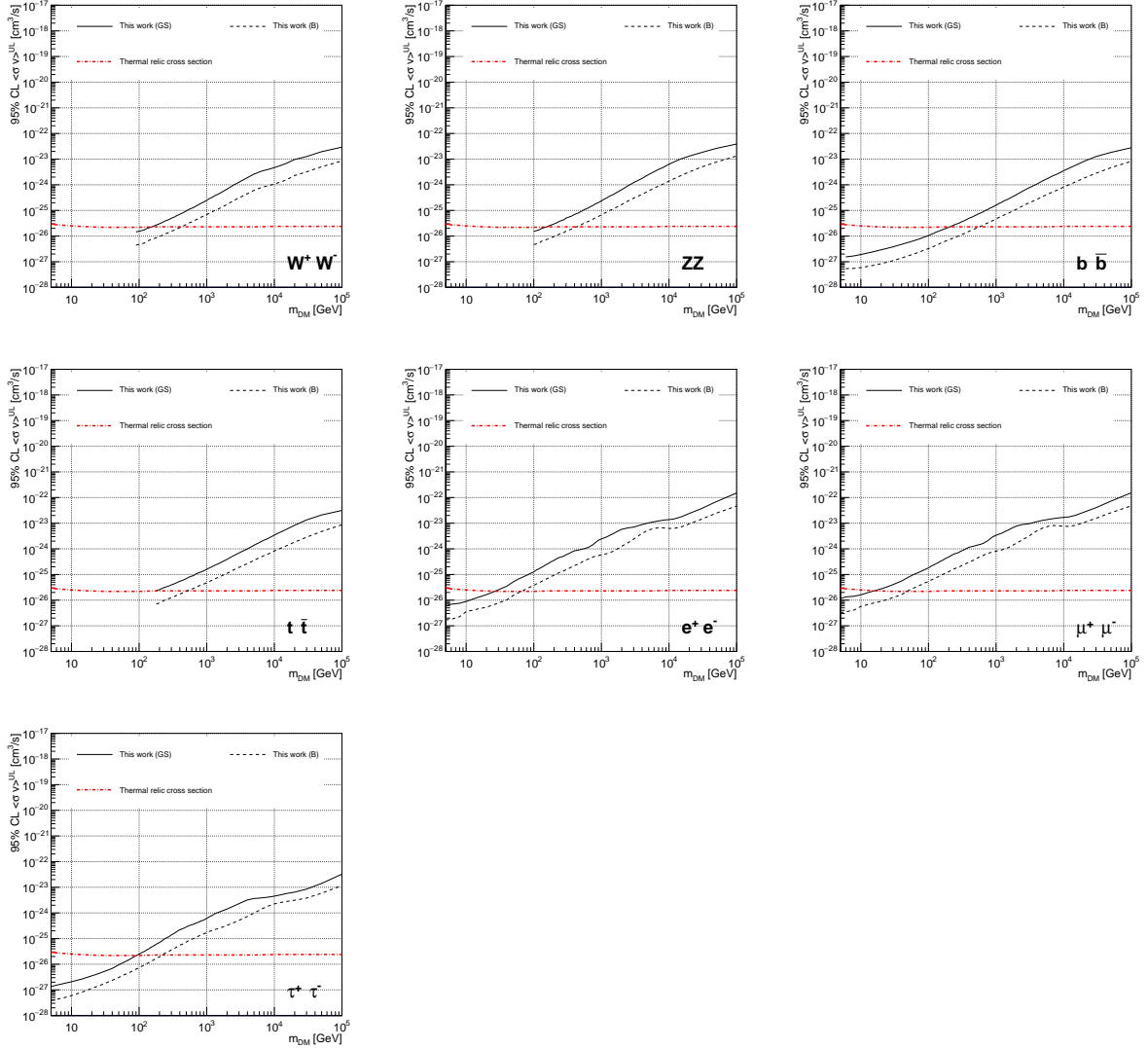


Figure 7.7 Comparisons of the combined limits at 95% confidence level for each of the eight annihilation channels when using the J factors from Ref. [32] (\mathcal{GS} set in Table 7.1), plain lines, and the J factor from Ref. [34, 38] (\mathcal{B} set in Table 7.1), dashed lines. The cross-section given by the thermal relic is also indicated [39].

Both dSphs pass almost overhead the HAWC detector, however Segue1 has the larger J-Factor between the two. Adjacent pixels to the central pixel will therefore contribute to the limits. This is the case for other dSph that are closer to overhead the HAWC detector.

Comparison plots for all sources and the combined limit can be found in the sandbox for the Glory Duck project.

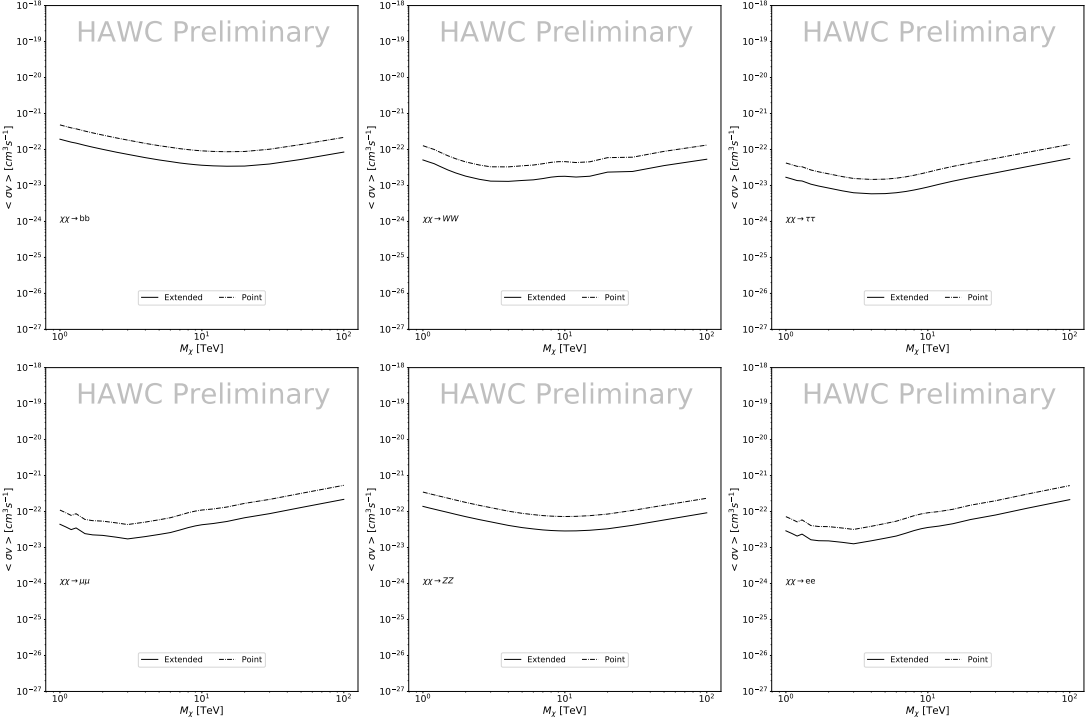


Figure 7.8 Comparisons of the combined limits at 95% confidence level for a point source analysis and extended source using [32] \mathcal{GS} J-factor distributions and PPPC [31] annihilation spectra. Shown are the limits for Segue1 which will have the most significant impact on the combined limit. 6 of the 7 DM annihilation channels are shown. Solid lines are extended source studies. Dashed lines are point source studies. Overall, the extended source analysis improves the limit by a factor of 2.

807 7.6.3 Impact of Pointing Systematic

808 During the analysis it was discovered that reconstruction of gamma-rays. Slides describing this
 809 systematic can be found here. Shown on the presentation is dependence on the pointing systematic
 810 on declination. New spatial profiles were generated for every dSph and limits were computed for
 811 the adjusted declination.

812 Section 7.6.3 demonstrates the impact of this systematic for all DM annihilation channels
 813 studied by HAWC. The impact is a tiny improvement, yet mostly identical, to the combined limits.

814 7.7 J-factor distributions

815 We show in this appendix a comparison between the J -factors computed by Geringer-Sameth
 816 *et al.* [32] (the \mathcal{GS} set) and the ones computed by Bonnivard *et al.* [34, 38] (the \mathcal{B} set). The
 817 \mathcal{GS} J -factors are computed through a Jeans analysis of the kinematic stellar data of the selected

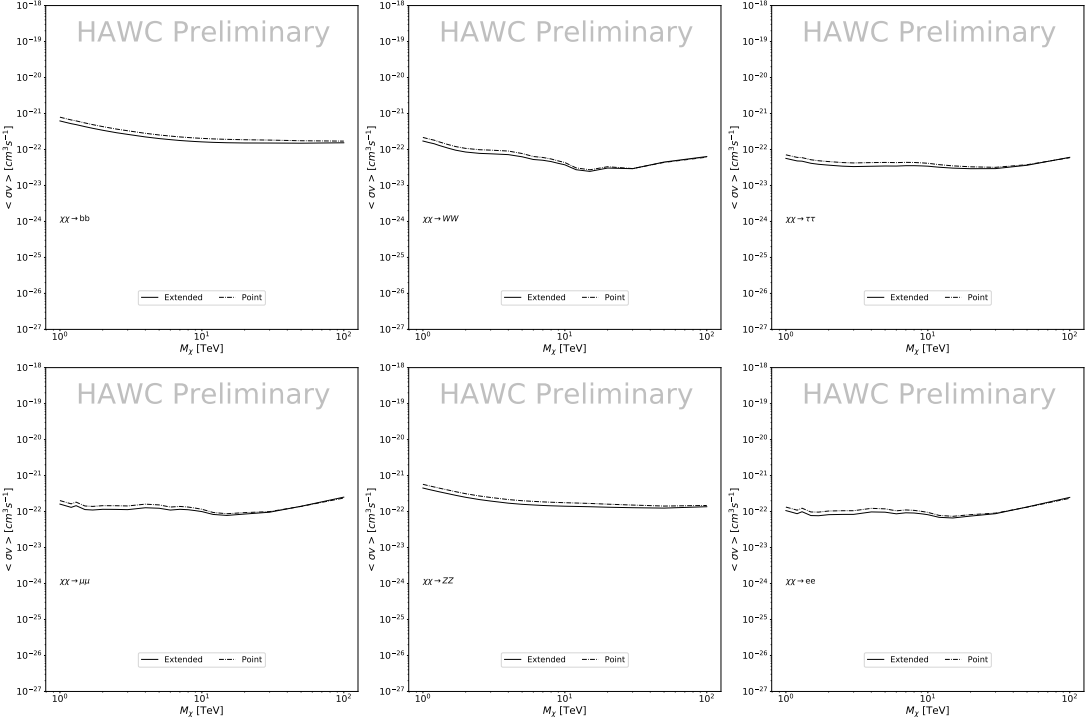


Figure 7.9 Same as Fig. 7.8 on Coma Berenices. This dSph also contributes significantly to the limit. The limits are identical in this case.

818 dSphs, assuming a dynamic equilibrium and a spherical symmetry for the dSphs. They adopted
 819 the generalized DM density distribution, known as Zhao-Hernquist, introduced by [40], carrying
 820 three additional index parameters to describe the inner and outer slopes, and the break of the
 821 density profile. Such a profile parametrization allows the reduction of the theoretical bias from
 822 the choice of a specific radial dependency on the kinematic data. In other words, the increase of
 823 free parameters with the use of the Zhao-Hernquist profile allows a better description of the mass
 824 density distribution of dark matter.

825 In addition, a constant velocity anisotropy profile and a Plummer light profile [41] for the stellar
 826 distribution were assumed. The velocity anisotropy profile depends on the radial and tangential
 827 velocity dispersions. However, its determination remains challenging since only the line-of-sight
 828 velocity dispersion can be derived from velocity measurements. Therefore, the parametrization of
 829 the anisotropy profile is obtained from simulated halos (see [42] for more details). They provide the
 830 values of the J -factors of regions extending to various angular radius up to the outermost member
 831 star.

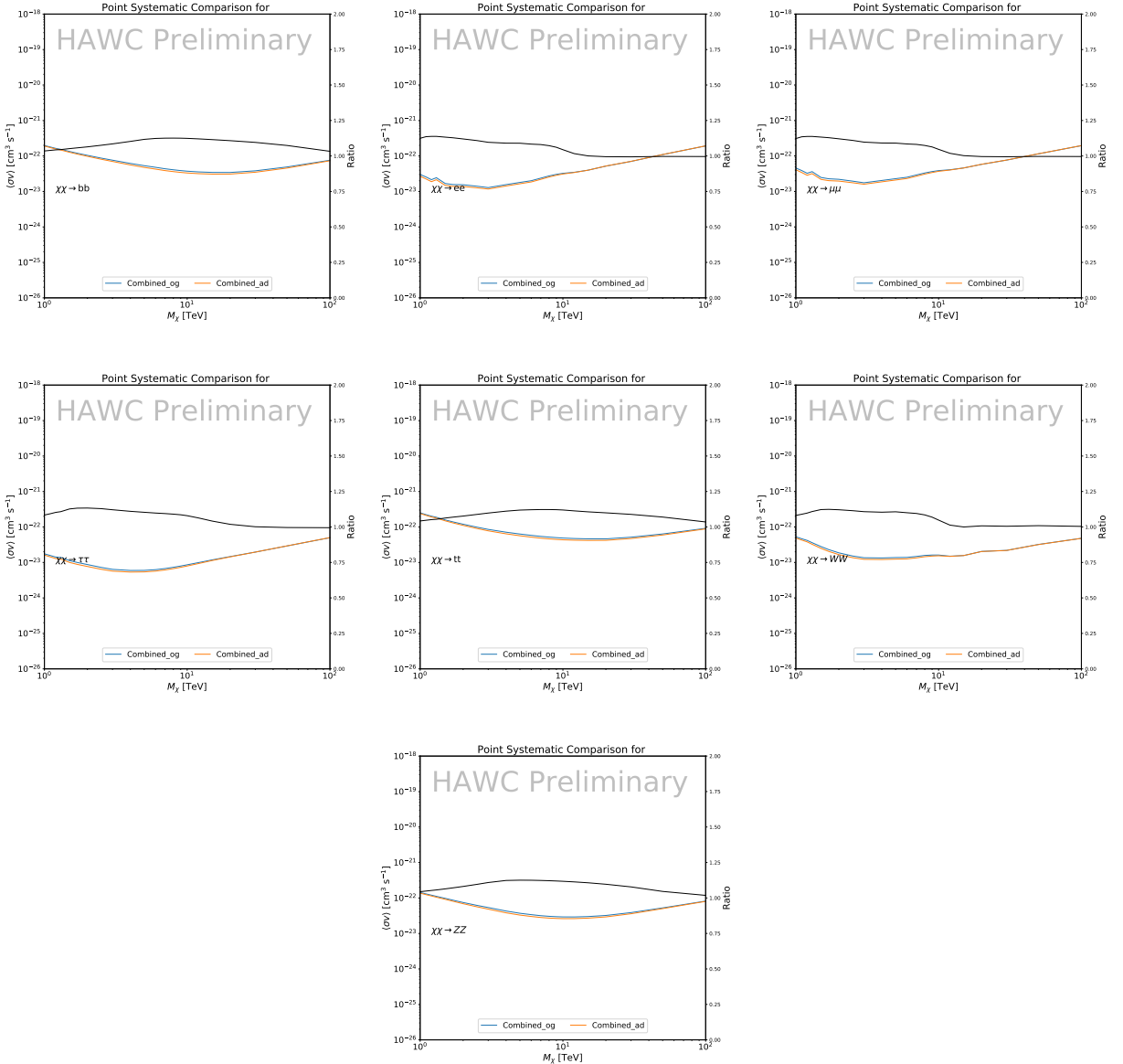


Figure 7.10 Comparison of combined limits when correcting for HAWC's pointing systematic. All DM annihilation channels are shown. The solid black line is the ratio between published limit to the declination corrected limit. The blue solid line or "Combined_og" represented the limits computed for Glory Duck. The solid orange line or "Combined_ad" represented the limits computed after correcting for the pointing systematic.

832 The \mathcal{B} J -factors were computed through a Jeans analysis taking into account the systematic
 833 uncertainties induced by the DM profile parametrization, the radial velocity anisotropy profile, and
 834 the triaxiality of the halo of the dwarf galaxies. They performed a more complete study of the dSph
 835 kinematics and dynamics than \mathcal{GS} for the determination of the J -factor. Conservative values of the

836 J -factors where obtained using an Einasto DM density profile [43], a realistic anisotropy profile
837 known as the Baes & Van Hese profile [44] which takes into account that the inner regions can be
838 significantly non-isotropic, and a Zhao-Hernquist light profile [40].

839 For both sets, J -factor values are provided for all dSphs as a function of the radius of the
840 integration region [32, 34, 38]. Table 7.1 shows the heliocentric distance and Galactic coordinates
841 of the twenty dSphs, together with the two sets of J -factor values integrated up to the outermost
842 observed star for \mathcal{GS} and the tidal radius for \mathcal{B} . Both J -factor sets were derived through a Jeans
843 analysis based on the same kinematic data, except for Draco where the measurements of [45] have
844 been adopted in the computation of the \mathcal{B} value. The computations for producing the \mathcal{GS} and \mathcal{B}
845 samples differ in the choice of the DM density, velocity anisotropy, and light profiles, for which the
846 set \mathcal{B} takes into account some sources of systematic uncertainties.

847 Figure 7.11 and Figure 7.12 show the comparisons for the J -factor versus the angular radius
848 for each of the 20 dSphs used in this study. The uncertainties provided by the authors are also
849 indicated in the figures. For the \mathcal{GS} set, the computation stops at the angular radius corresponding
850 to the outermost observed star, while for the \mathcal{B} set, the computation stops at the angular radius
851 corresponding to the tidal radius.

852 7.8 Discussion and Conclusions

853 In this multi-instrument analysis, we have used observations of 20 dSphs from the gamma-ray
854 telescopes Fermi-LAT, H.E.S.S., MAGIC, VERITAS, and HAWC to perform a collective DM
855 search annihilation signals. The data were combined across sources and detectors to significantly
856 increase the sensitivity of the search. We have observed no significant deviation from the null, no
857 DM, hypothesis, and so present our results in terms of upper limits on the annihilation cross section
858 for seven potential DM annihilation channels.

859 Fermi-LAT brings the most stringent constraints for continuum channels below approximately
860 1 TeV. the remaining detectors dominate at higher energies. Overall, for multi-TeV DM mass,
861 the combined DM constraints from all five telescopes are 2-3 times stronger than any individual
862 telescope for multi-TeV DM.

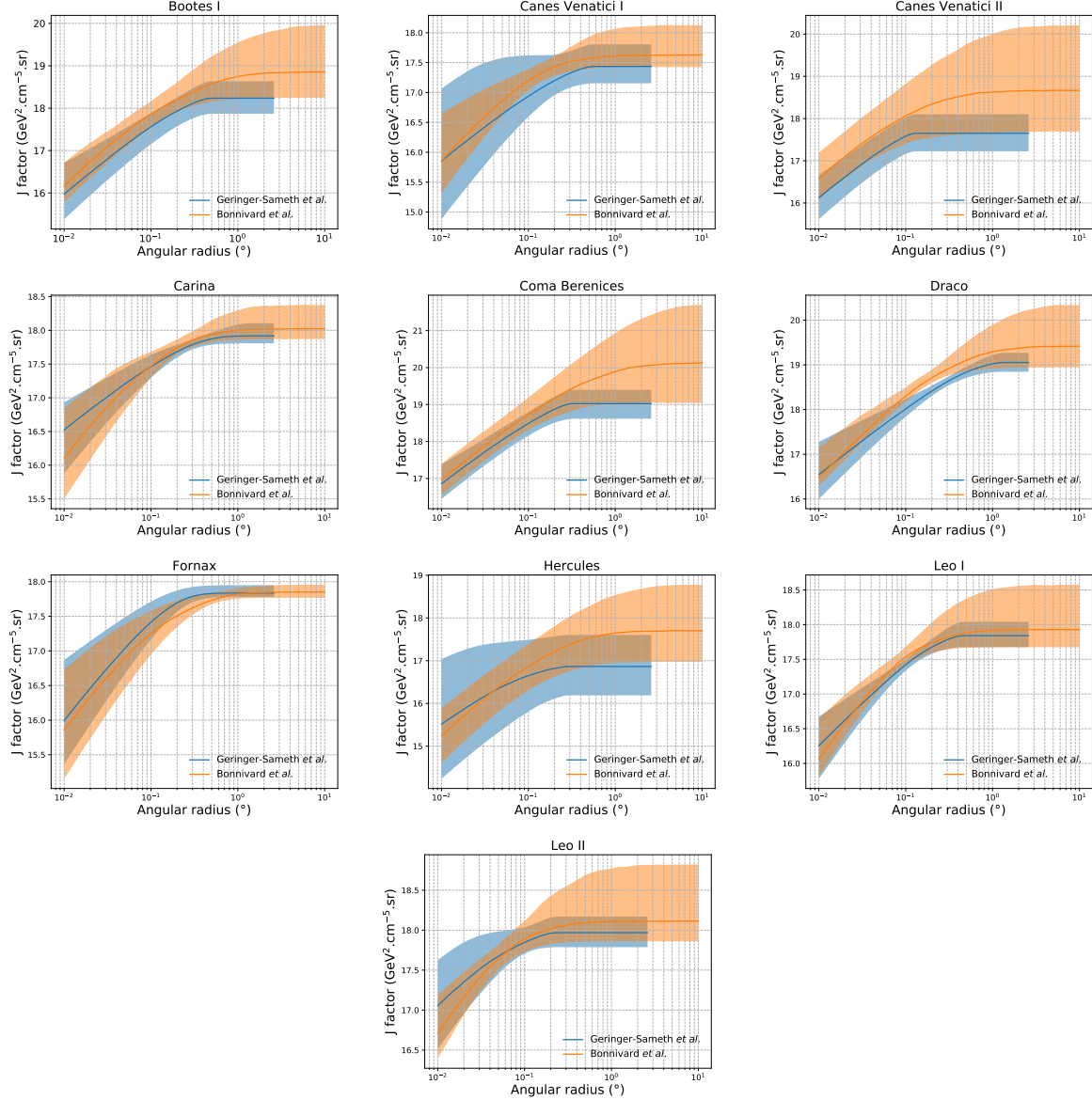


Figure 7.11 Comparisons between the J -factors versus the angular radius for the computation of J factors from Ref. [32] (\mathcal{GS} set in Table 7.1) in blue and for the computation from Ref. [34, 38] (\mathcal{B} set in Tab. 7.1) in orange. The solid lines represent the central value of the J -factors while the shaded regions correspond to the 1σ standard deviation.

863 Derived from observations of many dSphs, our results produce robust limits given the DM
 864 content of the dSphs is relatively well constrained. The obtained limits span the largest mass
 865 range of any WIMP DM search. Our combined analysis improves the sensitivity over previously
 866 published results from each detectors which produces the most stringent limits on DM annihilation
 867 from dSphs. These results are based on deep exposures of the most promising known dSphs with

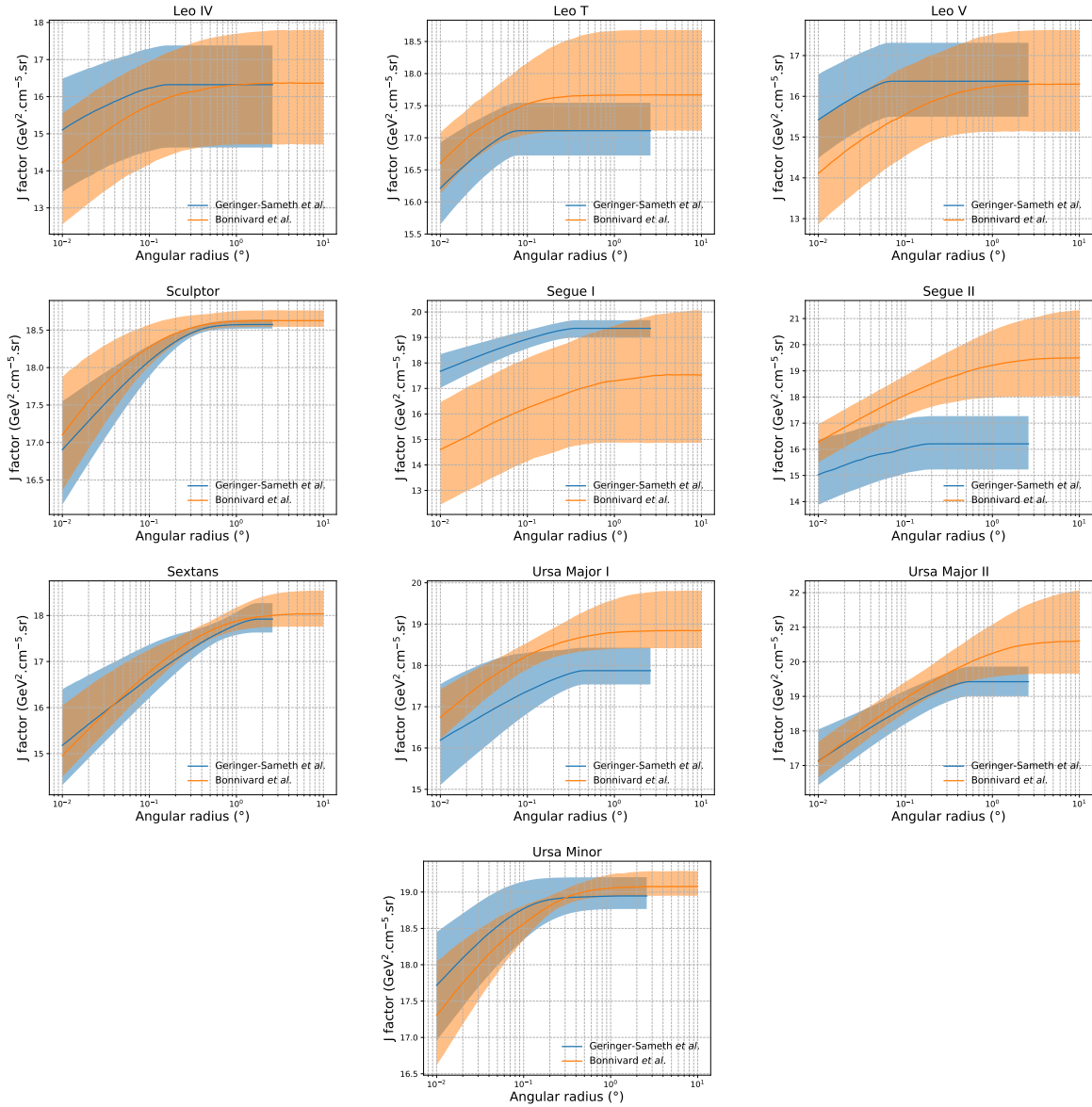


Figure 7.12 Comparisons between the J -factors versus the angular radius for the computation of J factors from Ref. [32] (\mathcal{GS} set in Tab. 7.1) in blue and for the computation from Ref. [34, 38] (\mathcal{B} set in Tab. 7.1) in orange. The solid lines represent the central value of the J -factors while the shaded regions correspond to the 1σ standard deviation.

the currently most sensitive gamma-ray instruments. Therefore, our results constitute a legacy of a generation of gamma-ray instruments on WIMP DM searches towards dSphs. Our results will remain the reference in the field until a new generation of more sensitive gamma-ray instruments begin operations, or until new dSphs with higher J -factors are discovered.

This analysis serves as a proof of concept for future multi-instrument and multi-messenger

873 combination analyses. With this collaborative effort, we have managed to sample over four orders
874 in magnitude in gamma-ray energies with distinct observational techniques. Determining the nature
875 of DM continues to be an elusive and difficult problem. Larger datasets with diverse measurement
876 techniques could be essential to tackling the DM problem. A future collaboration using similar
877 techniques as the ones described in this paper could grow even beyond gamma rays. The models we
878 used for this study include annihilation channels with neutrinos in the final state. Advanced studies
879 could aim to merge our results with those from neutrino observatories with large data sets. Efforts
880 are already underway to add data from the IceCube, ANTARES, and KM3NeT observatories to
881 these gamma-ray results.

882 From this work, a selection of the best candidates for observations, according to the latest
883 knowledge on stellar dynamics and modelling techniques for the derivation of the J -factors on the
884 potential dSphs targets, is highly desirable at the time that new experiments are starting their dark
885 matter programmes using dSphs. Given the systematic uncertainty inherent to the derivation of
886 the J -factors, an informed observational strategy would be to select both objects with the highest
887 J -factors that could lead to DM signal detection, and objects with robust J -factor predictions, i.e.
888 with kinematic measurements on many bright stars, which would strengthen the DM interpretation
889 reliability of the observation outcome.

890 This analysis combines data from multiple telescopes to produce strong constraints on astro-
891 physical objects. From this perspective, these methods can be applied beyond just DM searches.
892 Almost every astrophysical study can benefit from multi-telescope, multi-wavelength gamma-ray
893 studies. We have enabled these telescopes to study the cosmos with greater precision and detail.
894 Many astrophysical searches can benefit from multi-instrument gamma-ray studies, for which our
895 analysis lays the foundation.

CHAPTER 8

NU DUCK

896

CHAPTER 9

MULTITHREADING HAWC ANALYSES FOR DARK MATTER SEARCHES

BIBLIOGRAPHY

- 899 [1] Anne M. Green. “Dark matter in astrophysics/cosmology”. In: *SciPost Phys. Lect.*
 900 *Notes* (2022), p. 37. doi: [10.21468/SciPostPhysLectNotes.37](https://doi.org/10.21468/SciPostPhysLectNotes.37). URL: <https://scipost.org/10.21468/SciPostPhysLectNotes.37>.
- 902 [2] Bing-Lin Young. “A survey of dark matter and related topics in cosmology”. In: *Frontiers*
 903 *of Physics* 12 (Oct. 2016). doi: <https://doi.org/10.1007/s11467-016-0583-4>.
 904 URL: <https://doi.org/10.1007/s11467-016-0583-4>.
- 905 [3] Gianfranco Bertone, Dan Hooper, and Joseph Silk. “Particle dark matter: evidence,
 906 candidates and constraints”. In: *Physics Reports* 405.5 (2005), pp. 279–390. ISSN:
 907 0370-1573. doi: <https://doi.org/10.1016/j.physrep.2004.08.031>. URL:
 908 <https://www.sciencedirect.com/science/article/pii/S0370157304003515>.
- 909 [4] Gianfranco Bertone and Dan Hooper. “History of dark matter”. In: *Rev. Mod. Phys.*
 910 90 (4 Aug. 2018), p. 045002. doi: [10.1103/RevModPhys.90.045002](https://doi.org/10.1103/RevModPhys.90.045002). URL: <https://link.aps.org/doi/10.1103/RevModPhys.90.045002>.
- 912 [5] Fritz Zwicky. “The Redshift of Extragalactic Nebulae”. In: *Helvetica Physica Acta* 6.
 913 (1933), pp. 110–127. doi: [10.5169/seals-110267](https://doi.org/10.5169/seals-110267).
- 914 [6] Vera C. Rubin and Jr. Ford W. Kent. “Rotation of the Andromeda Nebula from a
 915 Spectroscopic Survey of Emission Regions”. In: *ApJ* 159 (Feb. 1970), p. 379. doi:
 916 [10.1086/150317](https://doi.org/10.1086/150317).
- 917 [7] K. G. Begeman, A. H. Broeils, and R. H. Sanders. “Extended rotation curves of spiral galax-
 918 ies: dark haloes and modified dynamics”. In: *Monthly Notices of the Royal Astronomical So-*
 919 *ciety* 249.3 (Apr. 1991), pp. 523–537. ISSN: 0035-8711. doi: [10.1093/mnras/249.3.523](https://doi.org/10.1093/mnras/249.3.523).
 920 eprint: <https://academic.oup.com/mnras/article-pdf/249/3/523/18160929/mnras249-0523.pdf>. URL: <https://doi.org/10.1093/mnras/249.3.523>.
- 922 [8] *Different types of gravitational lenses*. website. Feb. 2004. URL: <https://esahubble.org/images/heic0404b/>.
- 924 [9] Douglas Clowe et al. “A Direct Empirical Proof of the Existence of Dark Matter”. In: *apjl*
 925 648.2 (Sept. 2006), pp. L109–L113. doi: [10.1086/508162](https://doi.org/10.1086/508162). arXiv: [astro-ph/0608407](https://arxiv.org/abs/astro-ph/0608407)
 926 [*astro-ph*].
- 927 [10] Planck Collaboration and N. et. al. Aghanim. “Planck 2018 results I. Overview and the
 928 cosmological legacy of Planck”. In: *A&A* 641 (2020). doi: [10.1051/0004-6361/201833880](https://doi.org/10.1051/0004-6361/201833880). URL: <https://doi.org/10.1051/0004-6361/201833880>.
- 930 [11] Wayne Hu. *Matter Density Animation*. web. 2024. URL: <http://background.uchicago.edu/~whu/animbut/anim2.html>.

- 932 [12] Wenlong Yuan et al. “A First Look at Cepheids in a Type Ia Supernova Host with JWST”. in:
933 *The Astrophysical Journal Letters* 940.1 (Nov. 2022). doi: [10.3847/2041-8213/ac9b27](https://doi.org/10.3847/2041-8213/ac9b27).
934 URL: <https://dx.doi.org/10.3847/2041-8213/ac9b27>.
- 935 [13] Wendy L. Freedman. “Measurements of the Hubble Constant: Tensions in Perspective”. In:
936 *The Astrophysical Journal* 919.1 (Sept. 2021), p. 16. doi: [10.3847/1538-4357/ac0e95](https://doi.org/10.3847/1538-4357/ac0e95).
937 URL: <https://dx.doi.org/10.3847/1538-4357/ac0e95>.
- 938 [14] Jodi Cooley. “Dark Matter direct detection of classical WIMPs”. In: *SciPost Phys. Lect.*
939 *Notes* (2022), p. 55. doi: [10.21468/SciPostPhysLectNotes.55](https://doi.org/10.21468/SciPostPhysLectNotes.55). URL: <https://scipost.org/10.21468/SciPostPhysLectNotes.55>.
- 941 [15] “Search for new phenomena in events with an energetic jet and missing transverse momentum
942 in pp collisions at $\sqrt{s} = 13$ TeV with the ATLAS detector”. In: *Phys. Rev. D* 103
943 (11 July 2021), p. 112006. doi: [10.1103/PhysRevD.103.112006](https://doi.org/10.1103/PhysRevD.103.112006). URL: <https://link.aps.org/doi/10.1103/PhysRevD.103.112006>.
- 945 [16] *Jetting into the dark side: a precision search for dark matter*. website. July 2020. URL:
946 <https://atlas.cern/updates/briefing/precision-search-dark-matter>.
- 947 [17] Celine Armand et. al. “Combined dark matter searches towards dwarf spheroidal galaxies
948 with Fermi-LAT, HAWC, H.E.S.S., MAGIC, and VERITAS”. in: *Proceedings of Science*.
949 Vol. 395. Mar. 2022. doi: <https://doi.org/10.22323/1.395.0528>.
- 950 [18] Tracy R. Slatyer. “Les Houches Lectures on Indirect Detection of Dark Matter”. In: *SciPost*
951 *Phys. Lect. Notes* (2022), p. 53. doi: [10.21468/SciPostPhysLectNotes.53](https://doi.org/10.21468/SciPostPhysLectNotes.53). URL:
952 <https://scipost.org/10.21468/SciPostPhysLectNotes.53>.
- 953 [19] Christian W Bauer, Nicholas L. Rodd, and Bryan R. Webber. “Dark matter spectra from
954 the electroweak to the Planck scale”. In: *Journal of High Energy Physics* 2021.1029-8479
955 (June 2021). doi: [https://doi.org/10.1007/JHEP06\(2021\)121](https://doi.org/10.1007/JHEP06(2021)121).
- 956 [20] Riccardo Catena and Piero Ullio. “A novel determination of the local dark matter density”.
957 In: *Journal of Cosmology and Astroparticle Physics* 2010.08 (Aug. 2010), p. 004. doi:
958 [10.1088/1475-7516/2010/08/004](https://doi.org/10.1088/1475-7516/2010/08/004). URL: <https://dx.doi.org/10.1088/1475-7516/2010/08/004>.
- 960 [21] B. P. Abbott et al. “Observation of Gravitational Waves from a Binary Black Hole Merger”.
961 In: *Phys. Rev. Lett.* 116 (6 Feb. 2016), p. 061102. doi: [10.1103/PhysRevLett.116.061102](https://doi.org/10.1103/PhysRevLett.116.061102). URL: <https://link.aps.org/doi/10.1103/PhysRevLett.116.061102>.
- 963 [22] R. Abbasi et. al. “Observation of high-energy neutrinos from the Galactic plane”. In: *Science*
964 380.6652 (June 2023), pp. 1338–1343.
- 965 [23] NASA Goddard Space Flight Center. *Fermi’s 12-year view of the gamma-ray sky*. website.

- 966 2022. URL: <https://svs.gsfc.nasa.gov/14090>.
- 967 [24] Marco Cirelli et al. “PPPC 4 DM ID: a poor particle physicist cookbook for dark matter
968 indirect detection”. In: *Journal of Cosmology and Astroparticle Physics* 2011.03 (Mar.
969 2011), p. 051. doi: [10.1088/1475-7516/2011/03/051](https://doi.org/10.1088/1475-7516/2011/03/051). URL: <https://dx.doi.org/10.1088/1475-7516/2011/03/051>.
- 971 [25] W. B. Atwood et al. “The Large Area Telescope on the Fermi Gamma-Ray Space Telescope
972 Mission”. In: *apj* 697.2 (June 2009), pp. 1071–1102. doi: [10.1088/0004-637X/697/2/1071](https://doi.org/10.1088/0004-637X/697/2/1071). arXiv: [0902.1089](https://arxiv.org/abs/0902.1089) [astro-ph.IM].
- 974 [26] M. Ackermann et al. “Searching for Dark Matter Annihilation from Milky Way Dwarf
975 Spheroidal Galaxies with Six Years of Fermi Large Area Telescope Data”. In: *prl* 115.23,
976 231301 (Dec. 2015), p. 231301. doi: [10.1103/PhysRevLett.115.231301](https://doi.org/10.1103/PhysRevLett.115.231301). arXiv:
977 [1503.02641](https://arxiv.org/abs/1503.02641) [astro-ph.HE].
- 978 [27] Mattia Di Mauro, Martin Stref, and Francesca Calore. “Investigating the effect of Milky
979 Way dwarf spheroidal galaxies extension on dark matter searches with Fermi-LAT data”.
980 In: *Phys. Rev. D* 106 (12 Dec. 2022), p. 123032. doi: [10.1103/PhysRevD.106.123032](https://doi.org/10.1103/PhysRevD.106.123032).
981 URL: <https://link.aps.org/doi/10.1103/PhysRevD.106.123032>.
- 982 [28] A. U. Abeysekara et al. “Observation of the Crab Nebula with the HAWC Gamma-Ray
983 Observatory”. In: *The Astrophysical Journal* 843.1 (June 2017), p. 39. doi: [10.3847/1538-4357/aa7555](https://doi.org/10.3847/1538-4357/aa7555). URL: <https://doi.org/10.3847/1538-4357/aa7555>.
- 985 [29] A. Albert et al. “Dark Matter Limits from Dwarf Spheroidal Galaxies with the HAWC
986 Gamma-Ray Observatory”. In: *The Astrophysical Journal* 853.2 (Feb. 2018), p. 154. ISSN:
987 1538-4357. doi: [10.3847/1538-4357/aaa6d8](https://doi.org/10.3847/1538-4357/aaa6d8). URL: [http://dx.doi.org/10.3847/1538-4357/aaa6d8](https://dx.doi.org/10.3847/1538-4357/aaa6d8).
- 989 [30] Giacomo Vianello et al. *The Multi-Mission Maximum Likelihood framework (3ML)*. 2015.
990 arXiv: [1507.08343](https://arxiv.org/abs/1507.08343) [astro-ph.HE].
- 991 [31] Marco Cirelli et al. “PPPC 4 DM ID: a poor particle physicist cookbook for dark matter
992 indirect detection”. In: *Journal of Cosmology and Astroparticle Physics* 2011.03 (Mar.
993 2011). ISSN: 1475-7516. doi: [10.1088/1475-7516/2011/03/051](https://doi.org/10.1088/1475-7516/2011/03/051). URL: [http://dx.doi.org/10.1088/1475-7516/2011/03/051](https://dx.doi.org/10.1088/1475-7516/2011/03/051).
- 995 [32] Alex Geringer-Sameth and Matthew Koushiappas Savvas M. and Walker. “Dwarf galaxy
996 annihilation and decay emission profiles for dark matter experiments”. In: *Astrophys.
997 J.* 801.2 (2015), p. 74. doi: [10.1088/0004-637X/801/2/74](https://doi.org/10.1088/0004-637X/801/2/74). arXiv: [1408.0002](https://arxiv.org/abs/1408.0002)
998 [astro-ph.CO].
- 999 [33] Alex Geringer-Sameth, Savvas M. Koushiappas, and Matthew Walker. “DWARF GALAXY
1000 ANNIHILATION AND DECAY EMISSION PROFILES FOR DARK MATTER EXPERI-

- 1001 MENTS". in: *The Astrophysical Journal* 801.2 (Mar. 2015), p. 74. ISSN: 1538-4357. doi:
1002 [10.1088/0004-637x/801/2/74](https://doi.org/10.1088/0004-637x/801/2/74). URL: <http://dx.doi.org/10.1088/0004-637X/801/2/74>.
- 1004 [34] V. Bonnivard et al. "Spherical Jeans analysis for dark matter indirect detection in dwarf
1005 spheroidal galaxies - Impact of physical parameters and triaxiality". In: *Mon. Not. Roy.
1006 Astron. Soc.* 446 (2015), pp. 3002–3021. doi: [10.1093/mnras/stu2296](https://doi.org/10.1093/mnras/stu2296). arXiv:
1007 [1407.7822](https://arxiv.org/abs/1407.7822) [astro-ph.HE].
- 1008 [35] M. Ackermann et al. "Searching for Dark Matter Annihilation from Milky Way Dwarf
1009 Spheroidal Galaxies with Six Years of Fermi Large Area Telescope Data". In: *prl* 115.23,
1010 231301 (Dec. 2015), p. 231301. doi: [10.1103/PhysRevLett.115.231301](https://doi.org/10.1103/PhysRevLett.115.231301). arXiv:
1011 [1503.02641](https://arxiv.org/abs/1503.02641) [astro-ph.HE].
- 1012 [36] A. et al. Albert. "Searching for Dark Matter Annihilation in Recently Discovered Milky Way
1013 Satellites with Fermi-LAT". in: *Astrophys. J.* 834.2 (2017), p. 110. doi: [10.3847/1538-4357/834/2/110](https://doi.org/10.3847/1538-4
1014 357/834/2/110). arXiv: [1611.03184](https://arxiv.org/abs/1611.03184) [astro-ph.HE].
- 1015 [37] Mattia Di Mauro and Martin Wolfgang Winkler. "Multimessenger constraints on the dark
1016 matter interpretation of the Fermi-LAT Galactic Center excess". In: *prd* 103.12, 123005
1017 (June 2021), p. 123005. doi: [10.1103/PhysRevD.103.123005](https://doi.org/10.1103/PhysRevD.103.123005). arXiv: [2101.11027](https://arxiv.org/abs/2101.11027)
1018 [astro-ph.HE].
- 1019 [38] V. Bonnivard et al. "Dark matter annihilation and decay in dwarf spheroidal galaxies: The
1020 classical and ultrafaint dSphs". In: *Mon. Not. Roy. Astron. Soc.* 453.1 (2015), pp. 849–867.
1021 doi: [10.1093/mnras/stv1601](https://doi.org/10.1093/mnras/stv1601). arXiv: [1504.02048](https://arxiv.org/abs/1504.02048) [astro-ph.HE].
- 1022 [39] Gianfranco Bertone, Dan Hooper, and Joseph Silk. "Particle dark matter: evidence, can-
1023 didates and constraints". In: *Physics Reports* 405.5-6 (Jan. 2005), pp. 279–390. ISSN:
1024 0370-1573. doi: [10.1016/j.physrep.2004.08.031](https://doi.org/10.1016/j.physrep.2004.08.031). URL: <http://dx.doi.org/10.1016/j.physrep.2004.08.031>.
- 1026 [40] HongSheng Zhao. "Analytical models for galactic nuclei". In: *Mon. Not. Roy. Astron. Soc.*
1027 278 (1996), pp. 488–496. doi: [10.1093/mnras/278.2.488](https://doi.org/10.1093/mnras/278.2.488). arXiv: [astro-ph/9509122](https://arxiv.org/abs/astro-ph/9509122)
1028 [astro-ph].
- 1029 [41] H. C. Plummer. "On the Problem of Distribution in Globular Star Clusters: (Plate 8.)"
1030 In: *Monthly Notices of the Royal Astronomical Society* 71.5 (Mar. 1911), pp. 460–470.
1031 ISSN: 0035-8711. doi: [10.1093/mnras/71.5.460](https://doi.org/10.1093/mnras/71.5.460). eprint: <https://academic.oup.com/mnras/article-pdf/71/5/460/2937497/mnras71-0460.pdf>. URL:
1032 <https://doi.org/10.1093/mnras/71.5.460>.
- 1033 [42] Daniel R. Hunter. "Derivation of the anisotropy profile, constraints on the local velocity
1034 dispersion, and implications for direct detection". In: *JCAP* 02 (2014), p. 023. doi:
1035 [10.1088/1475-7516/2014/02/023](https://doi.org/10.1088/1475-7516/2014/02/023). arXiv: [1311.0256](https://arxiv.org/abs/1311.0256) [astro-ph.CO].

- 1037 [43] Barun Kumar Dhar and Liliya L. R. Williams. “Surface mass density of the Einasto family
1038 of dark matter haloes: are they Sersic-like?” In: *Mon. Not. Roy. Astron. Soc.* (2010). doi:
1039 [10.1111/j.1365-2966.2010.16446.x](https://doi.org/10.1111/j.1365-2966.2010.16446.x).
- 1040 [44] M. Baes and E. Van Hese. “Dynamical models with a general anisotropy profile”. In:
1041 *Astron. Astrophys.* 471 (2007), p. 419. doi: [10.1051/0004-6361:20077672](https://doi.org/10.1051/0004-6361:20077672). arXiv:
1042 [0705.4109](https://arxiv.org/abs/0705.4109) [astro-ph].
- 1043 [45] Matthew G. Walker, Edward W. Olszewski, and Mario Mateo. “Bayesian analysis of re-
1044 solved stellar spectra: application to MMT/Hectochelle observations of the Draco dwarf
1045 spheroidal”. In: *mnras* 448.3 (Apr. 2015), pp. 2717–2732. doi: [10.1093/mnras/stv099](https://doi.org/10.1093/mnras/stv099).
1046 arXiv: [1503.02589](https://arxiv.org/abs/1503.02589) [astro-ph.GA].